SciVerse ScienceDirect

Journal of Quantitative Spectroscopy and Radiative Transfer

A Stochastic Model for Density-Dependent Microwave Snow- and Graupel Scattering Coefficients of the NOAA JCSDA Community Radiative Transfer Model

Patrick G. Stegmann[a,*], Guanglin Tang[a], Ping Yang[a], Benjamin T. Johnson[b]

[a]*Department of Atmospheric Sciences, Texas A&M University, 3150 TAMU, 77840 College Station, TX, USA*

[b]NOAA Center for Weather and Climate Prediction, 5830 University Research Ct, 20740 College Park, MD, USA

Abstract

A structural model is developed for the single-scattering properties of snow and graupel particles with a strongly heterogeneous morphology and an arbitrary variable mass density. This effort is aimed to provide a mechanism to consider particle mass density variation in the microwave scattering coefficients implemented in the Community Radiative Transfer Model (CRTM). The stochastic model applies a bicontinuous random medium algorithm to a simple base shape and uses the Finite-Difference-Time-Domain (FDTD) method to compute the single-scattering properties of the resulting complex morphology.

Keywords: snow; graupel; CRTM; FDTD; bicontinuous random medium

1. Introduction

The Community Radiative Transfer Model (CRTM) is a flagship radiative transfer model of the U.S. National Oceanic and Atmospheric Adiministration (NOAA) and has been actively improved at the Joint Center for Satellite Data Assimilation (JCSDA). As described in the CRTM user guide by van Delst, (2013A) the CRTM is a fast scalar radiative transfer solver, whose primary purpose is its usage as a forward operator for satellite observational data assimilation in conjunction with the Global assimilation with Gridpoint Statistical Interpolation (GSI) code by Hu et al., (2016), in order to provide initial conditions and drift corrections for numerical weather prediction (NWP). Specific procedures for satellite data assimilation as conducted at the JCSDA are given for instance by Weng et al., (2003), while basic introductions to the topic of observational data assimilation can be found in Rodgers, (2000) and Kalnay, (2003). In this context, Rodgers,

* Corresponding author. Tel.: +1-979-862-4341.
E-mail address: pstegmann@tamu.edu

(2000) puts a stronger focus on the remote sensing aspect, while Kalnay, (2003) approaches the subject from the perspective of NWP. A more recent example, specifically including solid hydrometeors, has been published by Wood et al., (2014). The CRTM itself has been extensively validated in the past, by Chen et al., (2008), Yi et al., (2016) or Ding et al., (2011) in comparison with high accuracy solvers such as DISORT by Stamnes et al., (1988).

In addition to algorithms to deal with atmospheric absorption, the official CRTM release also includes two solvers to handle electromagnetic scattering by particles. In particular, these two solvers are the so-called "Advanced Doubling-Adding Method" (ADA) by Liu et al., (2006) and the Successive-Order-of-Interaction Radiative Transfer Model by Heidinger et al., (2005), with the ADA being the default solver. As detailed in the CRTM user guide by van Delst, (2013A), scattering particles are broadly categorized into aerosol and cloud particles, with optical property data sets for each category stored in a separate unformatted binary file. This study focuses on the cloud scattering properties retained as Look-Up tables (LUTs) in the CRTM CloudCoeff binary file. Due to its application for satellite data assimilation, the description of cloud particles in the CRTM aligns itself with cloud microphysical parameterizations used in NWP models, as described for instance by McCumber et al., (1991). The CRTM does not include a continuous, so-called spectral ice scheme, but uses a four-class, type 1 classification of cloud ice in the terminology of McCumber et al., (1991) instead. Aside from liquid water droplets, the CRTM distinguishes solid hydrometeors into cloud ice, and precipitating ice in the form of either snow, graupel, or hail. The distinguishing feature of the solid hydrometeor categories is their associated mass density, which is given in Table 1.

Table 1. Solid Hydrometeor Categories and associated densities in the CRTM Release 2.1.3

Category	**Density [g/cm^3]**
Cloud ice	0.900
Graupel & Hail	0.400
Snow	0.100

The original computations of the default single-scattering properties of the hydrometeors listed in Table 1 include certain inconsistencies, which are discussed in further detail in subsection 3.1 and section 4. A recent update of the CRTM ice optical properties has been provided by Yi et al., (2016), where the default ice optical properties are replaced by the so-called MODIS Collection 6 ice cloud optical properties (Platnick et al., (2017)) in the infrared and microwave regime and on the basis of the temperature dependent ice refractive index tabulated by Iwabuchi and Yang, (2011).

Consequently, this manuscript will focus on providing density-variable scattering properties for the remaining solid hydrometeor optical properties in the microwave regime, namely snow and graupel. The second section of this manuscript discusses the model proposed for the morphology of the graupel and snow scattering particles. Its third section describes the computation of the particle single-scattering properties and the fourth section deals with the corresponding bulk scattering properties and their adaption to the CRTM format. The fifth section investigates the changes brought about in the radiative transfer calculations involving scattering cloud layers, and the sixth section comprises the conclusion of the manuscript.

2. Particle Morphology Model

2.1. Bicontinuous Random Medium (BRM) Theory

As shown in Table 1, the crucial aspect distinguishing cloud ice, snow and graupel in the CRTM is the assumed bulk mass density. Consequently, the first and primary requirement for the morphological model is its ability to create a

scattering particle that can cover the entire range of bulk mass density as given in table 1. Moreover, observations of snow, graupel, and especially rimed snow documented in e.g. Pruppacher and Klett, (1978) or Kikuchi et al., (2013) show that these particles may often display a highly irregular, random structure that is often covered in rime for precipitating ice, which the model also needs to be able to reproduce. A natural response is to first look for a deterministic model that is able to reproduce the natural diffusive growth process of ice crystals in the atmosphere, such as the cellular automata of Gravner and Griffeath, (2009) or the subsequent parametric interface FEM model by Barrett et al., (2012). However, reproducing the full spectrum of possible solid precipitation shown by Kikuchi et al., (2013) using these methods is computationally not feasible in the scope of this project. Furthermore, random physical processes such as mesoscale surface roughness, riming, and turbulent convection cannot be considered using these methods alone. The importance of taking these processes into account in order to match the optical properties of real ice crystals has been demonstrated for instance for the case of surface roughness by Stegmann et al., (2016). In these cases, the chosen deterministic ice growth model would have to be supplemented by the approach of Zhang et al., (2016) for surface roughness, Criscione et al., (2015) for riming, and Wang, (2002) for turbulent convection, further increasing the computational complexity and strain of this method. Instead, a much simpler solution is the application of a bicontinuous random spatial partitioning scheme known from the theory of heterogeneous materials (see Sahimi, (2002) for an overview). The term bicontinuous in this context means that the two separated phases, which are ice and air for the case of snow and graupel, may display connected structures extending over the entire domain upon which the Bicontinuous Random Medium (BRM) algorithm is applied. This scheme had first been developed and applied to scalar scattering by a bulk medium by Berk, (1987) and Berk, (1991) as the so-called leveled-wave model. Later, the model has been applied to scattering of electromagnetic waves by particles by Ding et al., (2010) and Tang et al., (2017). Subsequently, the model has also been utilized by Xiong and Shi, (2014) in the context of polarized radiative transfer through layers of settled ground snow.

The basis of the BRM model as originally defined by Berk, (1987), is a finite superposition of stochastic standing cosine waves $S\left(\vec{r}\right)$. Its mathematical definition is given in Eq. (1), while an illustration can be found on the left hand side of Fig. 1.

$$S\left(\vec{r}\right)=\frac{1}{\sqrt{N}}\sum_{n=1}^{N}\cos\left(\vec{k}_n\cdot\vec{r}+\phi_n\right) \qquad (1)$$

Using differential geometric terminology, $S\left(\vec{r}\right)$ in Eq. (1) is a level set over a Euclidean manifold with coordinates $\vec{r}$, and as such it is a simplified stochastic special case of more general methods to track the dynamic evolution of interfaces as developed by Osher and Sethian, (1988). In Eq. (1), the integer N is the total number of superimposed cosine waves. The scalar $f_n \hat{\mathrm{I}} \left[0,2\rho\right)$ is the random phase shift associated with the n-th cosine wave $S_n\left(\vec{r}\right)$ and follows a uniform distribution. In the current study, an xorshift1024* pseudo-random number generator (PRNG) from the Xorshift class of PRNGs by Marsaglia, (2003) is used to obtain uniformly distributed random numbers. The 3D vector $\vec{k}_n=k_n\cdot\hat{k}_n$ is the wave vector of $S_n\left(\vec{r}\right)$. Its direction $\hat{k}_n$ is uniformly distributed on the unit sphere and its scaling wavenumber k_n determines the geometric properties and structural length scales of the BRM. Its selection is *a priori* arbitrary and as this work is primarily dealing with solid hydrometeors consisting of ice crystals, the gamma distribution suggested by Chen and

Chang, (1991) is selected. It should be noted that this choice is strongly dependent on the material under scrutiny. Berk, (1991) for instance used a shifted delta distribution to study water-oil microemulsions, i.e. only one specific wavenumber. In a notable analogy to the present study, the resulting morphologies obtained via the delta distribution bear a remarkable similarity to the structures computed by solving the deterministic Cahn-Hilliard PDE by Cahn and Hilliard, (1958), albeit at a fraction of the computational cost. As a consequence, the wavenumber may randomly take on any value in the interval $[0,\infty)$, under the sole condition that the frequency of occurrence of wavenumbers follows a gamma probability distribution function $p(k)$ as defined in Eq. (2).

$$p(k) = \frac{1}{\Gamma(b+1)} \frac{(b+1)^{b+1}}{\langle k \rangle} \left(\frac{k}{\langle k \rangle} \right)^{b} \exp\left(-(b+1) \frac{k}{\langle k \rangle} \right) \tag{2}$$

In Eq. (2), $\Gamma(x)$ is the Gamma function, $\langle k \rangle$ is the mean wavenumber, and b is a shape parameter related to the standard deviation of $p(k)$.

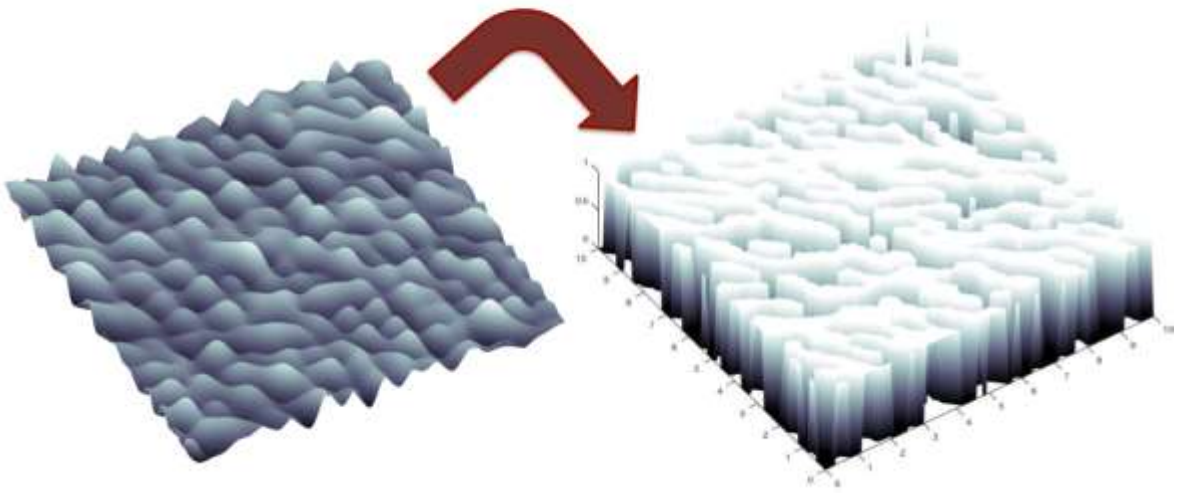

Fig. 1. Random superposition of cosine wave fields before (left) and after (right) the application of the ice-air threshold.

An algorithm for drawing pseudo-random numbers from a gamma probability distribution can be found for instance in Marsaglia and Tsang, (2000). After a realization of the random level set $S(\vec{r})$ has been drawn, the interface separating the two phases ice and air needs to be defined by choosing one specific level. This can be achieved by introducing a threshold level q given by Eq. (3).

$$q = erf^{-1}(1 - 2f_V) \tag{3}$$

Eq. (3) relates the threshold q of $S(\vec{r})$ to the volume fraction f_V of ice in the total volume on which the BRM model is applied via the inverse of the error function $erf^{-1}(x)$. The introduction of the threshold on a 2D example wave field is

illustrated in Fig. 1, with the resulting ice structure shown on the right side. The original field $S(\vec{r})$ is mapped to a new field $\tilde{S}(\vec{r})$, which is defined by Eq. (4).

$$S(\vec{r}) \xrightarrow{\theta} \tilde{S}(\vec{r}) = \begin{cases} 0 & if\ S(\vec{r}) < \theta \\ 1 & if\ S(\vec{r}) \geq \theta \end{cases} \tag{4}$$

This concludes the description of the BRM algorithm for generating random heterogeneous structures. It is evident from Eq. (3) that the bulk volume fraction f_V and thus mass density in the BRM model is a directly adjustable parameter. Thus the BRM scheme fulfills the original requirement of creating a particle with an arbitrary desired mass density. Furthermore, there is no *a priori* constraint on the distribution of the wavenumber $p(k)$, other than that it must be a true probability distribution. Consequently, a scattering particle model may be equipped with morphological features at any desired length scale, from coarse granularities down to small-scale surface roughness. As such, the BRM scheme has been selected as the model to create improved snow- and graupel microwave scattering properties for the CRTM, as it offers a broad flexibility at almost negligible computational cost.

2.2. Pristine Particle Shapes

In order to provide a pristine, fully solid base shape upon which the BRM algorithm can be applied, generic shapes for the snow and graupel categories of the CRTM have been chosen from parametric models given by Wang, (2002). The graupel particle model is assumed to be a body of revolution with a rotational symmetry axis along the x-direction, as depicted in Fig. 2.

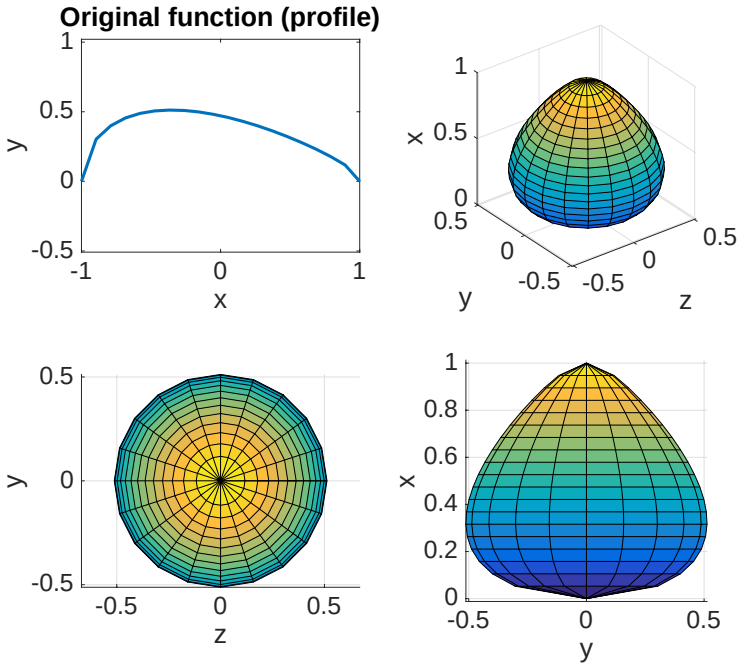

Fig. 2. A droplet-like body of revolution as a stand-in for a pristine graupel shape.

The basis for the shell of the body of revolution is the curve plotted in the upper left corner of Fig. 2. This curve is given by Wang, (2002) and its formulation is given again in Eq. (5) for the convenience of the reader.

$$y(x) = \pm a \times \sqrt{1 - \frac{x^2}{C^2}} \times \cos^{-1}\left(\frac{x}{/ \times C}\right) \tag{5}$$

In Eq. (5), the constants a, C and $/$ are parameters determining the height and aspect ratio of the particle, where a and C have the dimension of length, while $/$ is dimensionless. The function $\cos^{-1}(\times)$ is the arccosine. Similarly, the curve chosen for snow is a generic snowflake simulacrum depicted via an illustrative rendering in Fig. 3. Geometrically it is characterized by an aspect ratio of 10:1 and by its symmetry under transformations of the dihedral group D_6, the same as natural snowflakes and regular hexagonal prisms. This particular snowflake shape has been chosen due to its resemblance to natural and especially heavily rimed and irregular snowflakes as depicted by e.g. Pruppacher and Klett (1978). Furthermore, the high aspect ratio has been chosen as a marked contrast to the much more compact graupel model.

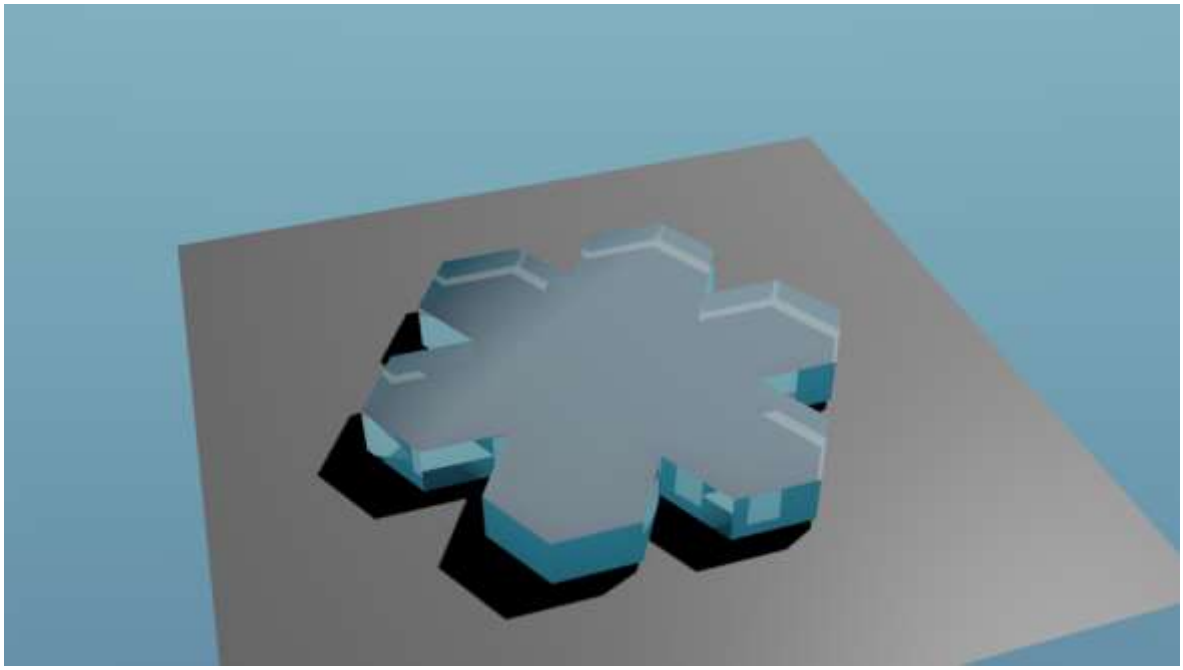

Fig. 3. Computer rendering of a generic hexagonal-prismatic snowflake shape used for the computation of the CRTM microwave coefficient single-scattering properties.

Before the application of the BRM algorithm, the largest dimension in units of length of the bulk model shape is normalized to one. This non-dimensionalization becomes necessary, as the mean wavenumber $\langle k \rangle$ and the shape parameter b in Eq. (2) are not dimensionless. Instead, $\langle k \rangle$ for instance has the dimension of an inverse length $\left[\frac{1}{L}\right]$ and consequently the application of the BRM algorithm for a fixed set of parameters on a non-dimensionless base shape such as the ones in Figs. 3 and 4 will result in qualitatively different outcomes for different particle sizes. In extreme cases, the BRM algorithm applied to a very small particle may produce geometric features at a scale larger than the particle itself, which will result in the particle either vanishing completely (zero density) or not showing any change at all (particle is entirely contained in the solid BRM structure), depending on the stochastic realization of the BRM field $\tilde{S}(\vec{r})$ as shown e.g. on the right side of Fig. 1. This situation is undesirable, of course, as it also does not allow to correctly adjust the particle density, and it is entirely avoided by normalizing the base particle size. This normalization process eventually leads to an internal structure with different length scales for particles at different sizes. This does not conform with the microphysics of how these structures evolve, both in the case of supercooled water and diffusive crystal growth, however, it ensures that the scattering particle always has the desired mass density.

2.3. Practical Application of the BRM to Scattering Particles

Given the postulated graupel and snow base shapes shown in Figs. 2 and 3, further processing is enabled by the triangulation of the surface of these shapes and saving the surface triangulation in Standard Tesselation Language (STL) file format (see Hiller and Lipson, (2009) for a description of this common file format).

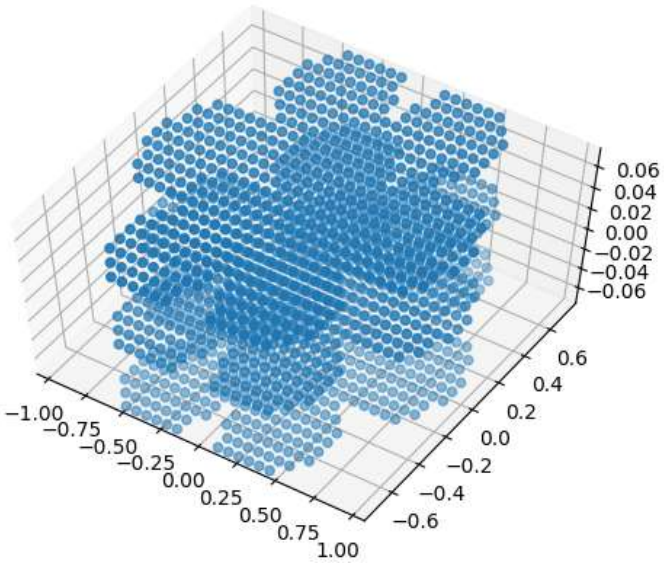

Fig. 4. Discrete representation of the snowflake geometry of Fig. 3 on a cubic lattice. On display is a low-resolution discretization for better visibility of the spatial structure. Each vertical layer is detached, so as to improve the visibility of the layer below.

As further detailed in section 3, the single-scattering properties of the snow and graupel ensemble will be calculated using fully numerical methods which require the discretization of the particle shapes, effectively replacing the particle shape model by a regular cubic computational lattice. As a first step of this discretization process, a set of points on a regular lattice is created inside an arbitrary volume that entirely contains the scattering particle. For each point, a standard algorithm from computational geometry is applied to check, whether the grid point is inside the domain bounded by the surface triangulation of the particle. The resulting reduced set of lattice of points for a snowflake is shown in Fig. 4 as an example. Subsequently, the BRM algorithm comprised of Eqs. (1) through (4) is executed for a suitable wavenumber distribution $p(k)$ to produce a desired BRM field $\tilde{S}(\vec{r})$ on the lattice domain. The resulting field now is evaluated at each remaining lattice point $\vec{r}_{lattice}$ using Eq. (4) and the point is only kept if $\tilde{S}(\vec{r}_{lattice})$ evaluates to 1. A result of an example run of this procedure is shown in Fig. 5 and should be contrasted with the regular particle lattice in Fig. 4 before the application of the BRM scheme. On the basis of this discretization the single-scattering properties of the snow and graupel particles can now be calculated.

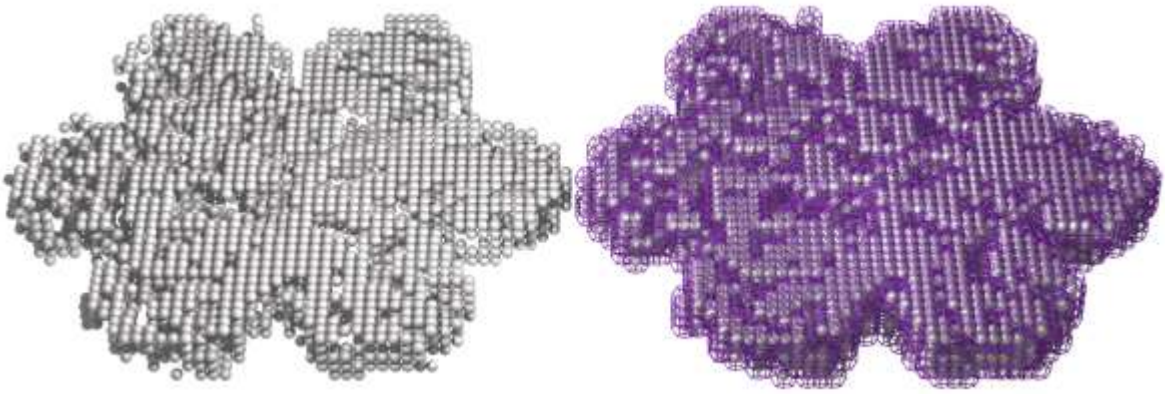

Fig. 5. Rendering of the regular cubic lattice resulting from the discretization of the solid shape shown in Fig. 3, superimposed with the BRM field (left) and rendering of the associated Voronoi tessellation (right). The resulting lattice is a single realization of a BRM field $\tilde{S}(\vec{r})$ with parameters $\langle k \rangle = 2.5$, b = 10 and $f_V = 0.6$.

As explained in subsection 2.1, the continuous BRM field itself by definition does not allow micro-components that are disconnected from the main particle. As shown in Fig. 5, however, the discretization process may introduce grid points that appear to be disconnected from the bulk of the particle. It is nevertheless important to keep in mind that the object shown in Fig. 5 is a computational lattice, and not a continuous physical particle anymore. The issue of particle connectivity becomes irrelevant at this point of the analysis and the remaining criterion to judge the soundness of the model is the convergence of its computed optical properties, as discussed in further detail in subsection 3.3.

3. Computation of Single-scattering Properties

In Section 3, the computation of the full Müller-matrix for BRM particles in the Microwave regime is discussed. While all necessary single-scattering data for a vector radiative transfer code are available, the CRTM currently only allows scalar computations and as such the polarized scattering data is not included in the CRTM LUTs for any kind of scattering particle.

3.1. Computational Details of the Default CRTM Scattering Properties

Following Liu and Weng, (2006) or Chen et al., (2008), it is stated in both publications that the single-scattering properties for the CRTM solid hydrometeors listed in Table 1 have been obtained from scattering tables based on Lorenz-Mie calculations (see Mie, (1908) for the original solution of Maxwell's equations for a spherical dielectric scatterer) and these tables originate from a combination of different single-scattering properties from different publications, including Simmer, (1994), Yang and Liou, (1995), Macke et al., (1996), Mishchenko et al., (2000), Baum et al., (2005), and Yang et al., (2005). However, it can be seen immediately that out of the mentioned publications, only Simmer, (1994) applies Lorenz-Mie computations to microwave scattering of hydrometeors and in section 4 of this manuscript, further arguments will be presented that the origin of the CRTM Release 2.1.3 default cloud scattering properties may not be found in the above mentioned references, or some serious inconsistency has taken place during the processing of the scattering data into a CRTM input format.

3.2. Single-Scattering Database Calculation Outline

As stated in van Delst, (2013A), the default radiative transfer (RT) solver of the CRTM is the so-called "Advanced Doubling-Adding Method" (ADA), which is a one-dimensional, scalar RT method developed by Liu and Weng, (2006). Furthermore, the number of streams in a CRTM Release 2.1.3 calculation is automatically adjusted based on the particle Mie size parameter, with a maximum of 16 streams. Following the theoretical description of the algorithm in Liu and Weng, (2006), this particular radiative transfer solver requires the extinction coefficient, single-scattering albedo and phase function to in order to include a layer with light scattering properties in a CRTM radiative transfer calculation. In the CRTM, these scattering properties for cloud layers including ice, snow, and graupel are read from the corresponding binary data file and stored in a custom Fortran data type called ***CloudCoeff_type***. Due to the rigid definition of the ***CloudCoeff_type*** data type in the CRTM source code by van Delst, (2013B), there is only a fixed number of effective scattering particle sizes and frequencies of the incident electromagnetic field defined. Furthermore, the definition of ***CloudCoeff_type*** makes it clear that the effective sizes are identical for all solid precipitation particles listed in Table 1. From an application point of view this is inconvenient, as it might be deemed necessary to have e.g. smaller sizes for ice crystals and larger sizes for graupel and ground snow. Both frequencies and effective sizes included in the CRTM Release 2.1.3 cloud scattering coefficients have not been published in any place before and are thus listed in Table 2 and 4 respectively (data extracted from van Delst, (2013B)).

Table 2. Frequencies of incident electromagnetic radiation included in the CRTM Release 2.1.3 cloud scattering coefficients (source: van Delst, (2013B)).

CRTM Frequency [GHz]
1.4
6.8
6.92
10.7
18.7
19.35
21.3
22.235
23.8

31.4
36.5
37
50.3
52.8
53.5
54.4
54.94
55.5
57.29
59.4
60.67
63.28
70
75
85
89
91.65
150
157
183.31
190.31

Consequently, a database of single-scattering properties needs to be computed for all the frequencies listed in Table 2 and all the effective sizes in Table 3 based on the BRM particle models described in section 2. Based on the data given in Tables 2 and 3, one can compute the maximum Mie size parameter x_{Mie} of the database as ratio of the maximum particle size divided by shortest incident wavelength times pi.

Table 3. CRTM Release 2.1.3 cloud scattering effective sizes (source: van Delst, 2013B).

CRTM Effective Size D_{eff} [µm]	**Corresponding size distribution exponent Γ_g [1/µm]**
5	0.19
15	0.054
30	0.026
50	0.0018
100	0.0013
300	7.754e-4
500	6.0311e-4
800	4.8413e-4
1000	4.3641e-4
1500	3.5982e-4

The resulting maximum size parameter, with $D_{\max}$ always being defined as the largest length scale of the scattering particle, is roughly $x_{Mie} = \frac{\pi D_{\max}}{\lambda_{\min}} \approx \pi \approx 3.14159...$ and thus of order one. It should be noted that in the following all size parameters are defined based on the particle maximum dimension. As a result of this estimate, it becomes clear that the database will largely be located in the Rayleigh scattering regime. The remainder of the database is of such a low size parameter that exact methods for the solution of Maxwell's equations can be applied easily. As a first option, the semi-analytic Invariant Imbedding T-Matrix (IIT-M) method by Bi et al., (2013) may be used. However, due to the highly irregular structure of a BRM particle, the rate of convergence of the IIT-M method is drastically impeded, to the point that other methods become more efficient for the calculation of a database such as this one. As the model particle *volumes* are stochastically irregular, the numerically exact Finite Difference Time Domain (FDTD) scattering code of Yang and Liou, (1996) has ultimately been chosen for the calculation of the single-scattering properties of the BRM snow and graupel particles. This code is based on the classical FDTD scheme of Yee, (1966), which is in itself a special case of the more general Finite Integration Technique (FIT) by Weiland, (1977) for regular cubic grids. Consequently, the FDTD employs a staggered grid to achieve second order accuracy in space and leapfrog integration to likewise achieve second order accuracy in time, as well as symplectic phase space area conservation (see Weiland, (1984) for a proof of the latter property). The Perfectly Matched Layer (PML) absorbing boundary condition by Chew and Weedon, (1994) is used to truncate the computational domain.

For all calculations, the material out of which the scattering particles consist was assumed to be water ice in its common form I_h. The most recent and comprehensive database for the temperature-dependent refractive index spectrum of ice I_h as of 2017 is available from Iwabuchi and Yang, (2011) and the appropriate refractive index at each necessary temperature and frequency is obtained via bilinear interpolation as a preprocessing step before the initialization of the actual FDTD calculation.

3.3. FDTD Convergence and Cross-Validation

As a fully numerical method, the responsibility to ensure that the FDTD scheme produces sensible results rests with the user. Out of this necessity, a grid resolution convergence study and cross-validation of the FDTD output with other methods has been performed before the computation of the full CRTM database was undertaken. All single-scattering results are averaged over the scattering particle orientation in space and thus cases where a preferential orientation may exist are deliberately excluded from this study. Applying a Householder transformation with respect to the scattering plane to a configuration of grid points such as the one shown in Fig. 5 in half of all cases reduces the number of independent Müller matrix elements in the computation that are nonzero to 6, as explained by van de Hulst, (1981). This becomes necessary, as the BRM particles discussed in this work are generally not their own mirror particle due to a lack of symmetry.

The convergence test case uses the snowflake model shape depicted in Fig. 3 with a maximum size of D_{max} = 6 mm and a temperature of T_{ice} = 270 K. For the incident electromagnetic radiation, the highest possible frequency had been chosen, i.e. 190 GHz and the particle volume fraction f_V was fixed at 60 % in order to obtain a sufficiently complex internal BRM structure. All other BRM parameters are the same as in Fig. 5. This particular set of calculation input parameters is chosen as it represents the largest size parameter and the sharpest refractive index contrast considered in this study. Thus the chosen test case represents the set of parameters with the slowest convergence rate. The results of the convergence study are shown

in Figs. 6 and 7. The figures show the computed single-scattering albedos ϖ and the sensitive phase function values at the exact backscattering angle $P_{11}(\theta=\pi)$ together with an extrapolation for different grid resolutions. It is understood that the extrapolated values in Fig. 7 may not coincide with the actual convergence distribution.

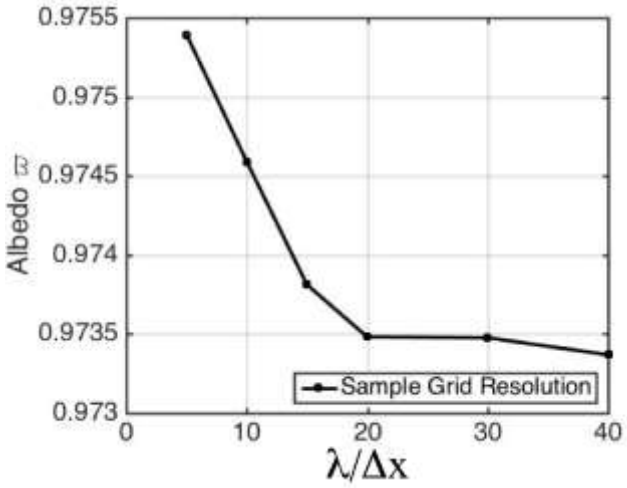

Fig. 6. Single-scattering albedo result of the FDTD convergence study.

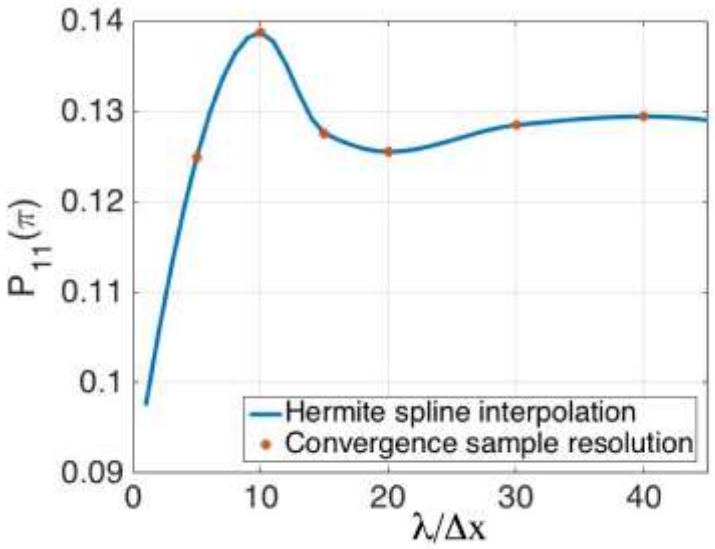

Fig. 7. Exact backscattering direction phase function element behavior during the FDTD convergence study.

The results suggest that for a large-scale database calculation, a resolution of $\frac{l}{\Delta x}=35$ grid-points per wavelength of the incident radiation provides sufficient accuracy and a further increase in the number of grid-points will be met with diminishing returns. Here, Δx is the grid spacing of the FDTD grid in units of length, not to be confused with the Mie size parameter x_{Mie}. However, in practice a maximum principle needs to be applied for a BRM particle. Given the algorithm outlined in section 2, it needs to be ensured that the BRM morphology is resolved with sufficient accuracy as well. For a

given BRM realization, whose geometry and smallest scales are sufficiently resolved by N_{BRM} grid points, this leads to the following requirement for the number of FDTD grid-points N_{FDTD} for the calculation of the CRTM cloud scattering properties:

$$N_{FDTD} = \max\left(35, N_{BRM}\right) \tag{6}$$

After criteria for the convergence of the FDTD calculations have been established, a cross-validation with analytical Mie- and T-Matrix results for a solid spherical particle is performed, as well as a comparison with the fully numerical Discrete-Dipole Approximation (DDA) results for the non-spherical model particle shown in Fig. 5. The results from the analytical comparison are shown in Fig. 8, and the comparison for the numerical case is given in Fig. 9. For the spherical validation case, a temperature of T_{ice} = 270 K, a diameter of D_{max} = 1.5 mm and a frequency 190.31 GHz has been chosen. The resulting complex refractive index for ice is $n_{ice} = 1.7838 + i \times 0.00416$. Figure 8 shows the comparison between a T-Matrix phase function P_{11} obtained using the Tsym 5.2 code from Kahnert, (2005), a freely available MS Windows Mie solution calculator program MiePlot v4.607 by Laven, (2003) and based on the BHMIE algorithm by Bohren and Huffman, (1993), and two FDTD calculation results with a resolution of 35 and 50 grid-points per wavelength respectively. It can be seen that both the high-and intermediate resolution FDTD phase functions are almost indistinguishable from the T-Matrix- and Mie solution. The Tsym calculations have been performed with 36 matrix elements and $q' j = 16' 4$ quadrature points for the evaluation of the surface integrals. For the analytical comparison, the BRM algorithm has of course not been applied.

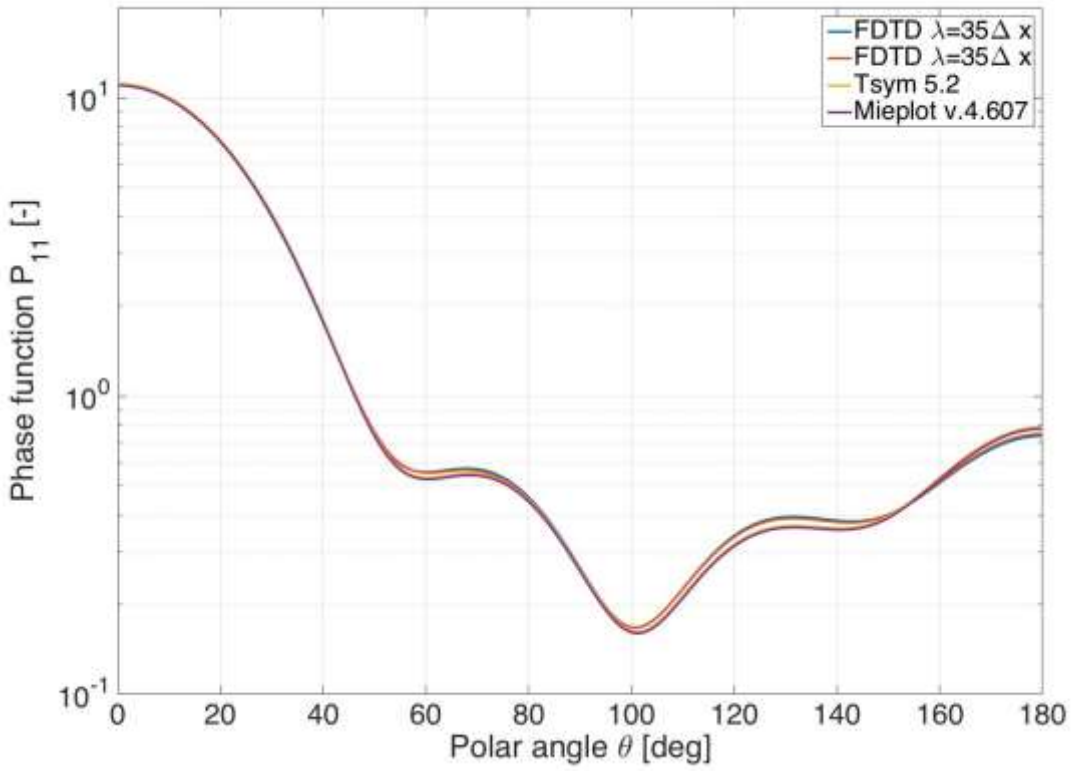

Fig. 8. Comparison of FDTD- with T-Matrix and Mie phase function results.

For the case of a non-spherical particle including the BRM approach, a numerical cross-validation of the FDTD scheme with the Amsterdam DDA code by Yurkin et al., (2007) has been performed. The results are shown in Fig. 9 and all physical parameters are identical to the Mie validation case, with the exception of the particle shape and the BRM parameters. The scattering particle is a snowflake realization with the same BRM parameters, as the one in Fig. 5. As can be seen in Fig. 9, there is reasonable agreement between the A-DDA and the FDTD phase functions even for a moderate-resolution FDTD grid and the disagreement is most pronounced in the sensitive backward scattering region. Overall, the outcome of the comparison is very similar to the results in the spherical case.

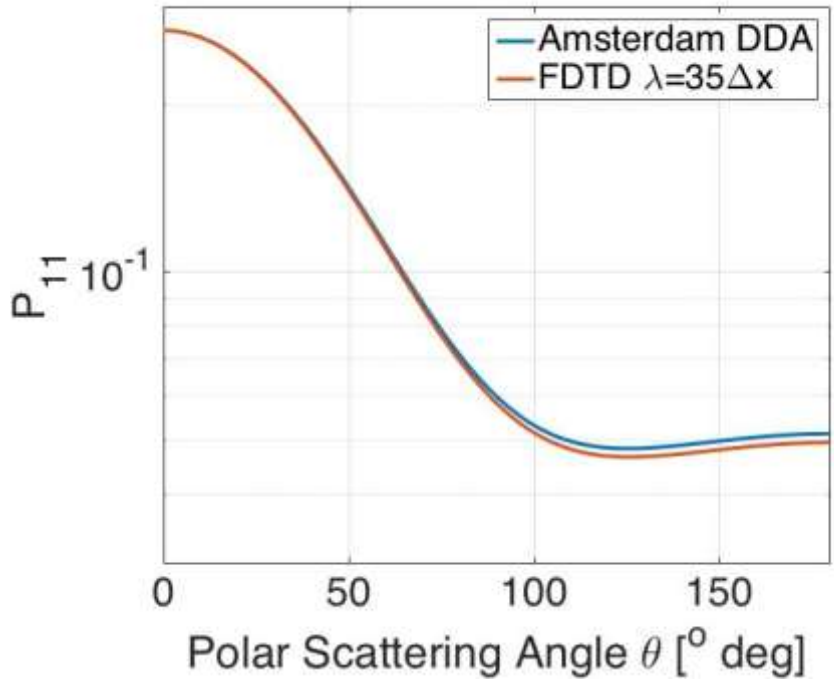

Fig. 9. Comparison of FDTD- and A-DDA results.

However, as the A-DDA is again based on a cubic discretization of the scattering particle volume created using the algorithm outlined in section 2, it needs to follow a similar requirement as the FDTD scheme with Eq. (6). Draine and Flatau, (1994) give the recommendation in Eq. (7) for the resolution of DDA computations in general.

$$N_{DDA} > \frac{4p^2}{3l}\left|n_{ice}\right| D_{\max} \qquad (7)$$

In Eq. (7), N_{DDA} is the number of "dipoles" in one coordinate direction, l is the wavelength of the incident electromagnetic radiation, n_{ice} the complex refractive index of ice and $D_{\max}$ the maximum size of the particle in the corresponding coordinate direction. As the DDA is only used for validation calculations and computational requirements are low due to the small size parameter, a resolution of 50 "dipoles" in each coordinate direction has been chosen, which is comfortably larger than the estimate obtained from Eq. (7) for the given set of calculation parameters.

3.4. Single-scattering Property results and Influence of Density Variation

Utilizing the validated FDTD code, a database of single-scattering properties for the CRTM frequencies and effective sizes given in Tables 2 and 3 respectively are computed. The CRTM also allows to consider the influence of different atmospheric temperature conditions on the scattering properties. Nevertheless, this is limited to liquid water droplets only and the narrow available temperature range is given in Table 4. For solid hydrometeors, changing temperature-dependent scattering properties is only possible through manual replacement of the CloudCoeff binary data file, thus making a temperature-adaptation at runtime impossible. As part of the present study a set of CRTM cloud scattering coefficients for both 270 K and 160 K temperature has been computed. However, assessing the full impact of ice cloud temperature on the optical properties of snow, as has been done to a limited extent by Yi et al., (2016) through consideration of a temperature-dependent refractive index, is beyond the scope of the present study.

Table 4. CRTM cloud temperatures currently available in the CRTM Release 2.1.3 CloudCoeff binary data files.

CRTM Temperatures [K]
263.16
273.16
282.00

The influence of the scattering particle density adjusted through the BRM scheme has already been investigated in a preliminary study by Tang et al., (2017). It has been found that the influence of the density variation on the phase function of graupel model particles is considerable and for the calculation of CRTM graupel scattering properties, the BRM volume ratio has been adjusted to $f_V = 0.4$. For the present case of a thin snow particle model with a high aspect ratio this effect, however, has not been studied yet. In order to perform the sensitivity study, a snow particle with maximum dimension of 1 mm and temperature 270 K is chosen, which is irradiated by a 190 GHz plane wave. As the size parameter of the scattering problem is at the higher end of the possible values relevant for the CRTM, the complex BRM morphology of the snow particle is expected to play a more prominent role. With all other parameters held fixed, the volume ratio of the particle is allowed to vary between 20 and 100 percent. The corresponding single-scattering results are shown in Figs. 10a to 10b.

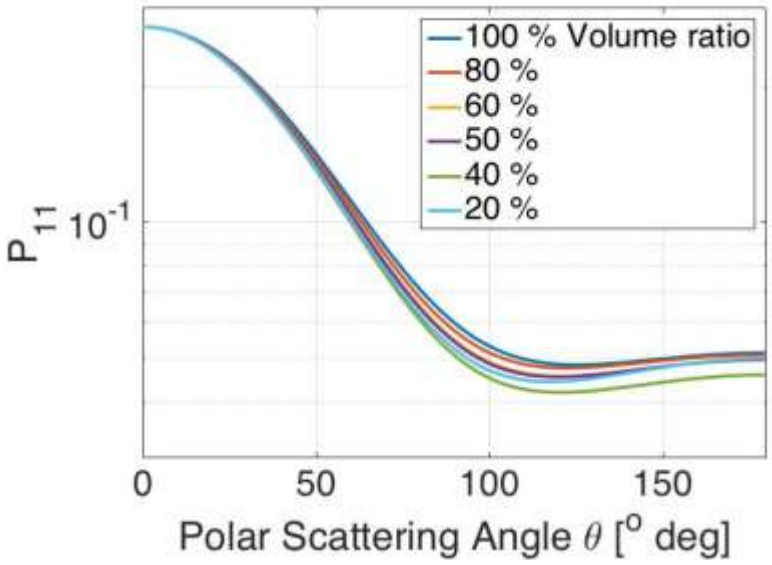

Fig. 10a. Influence of particle density on the phase function P_{11} for a snow particle with 1 mm size at 270K and illuminated by 190 GHz microwave radiation.

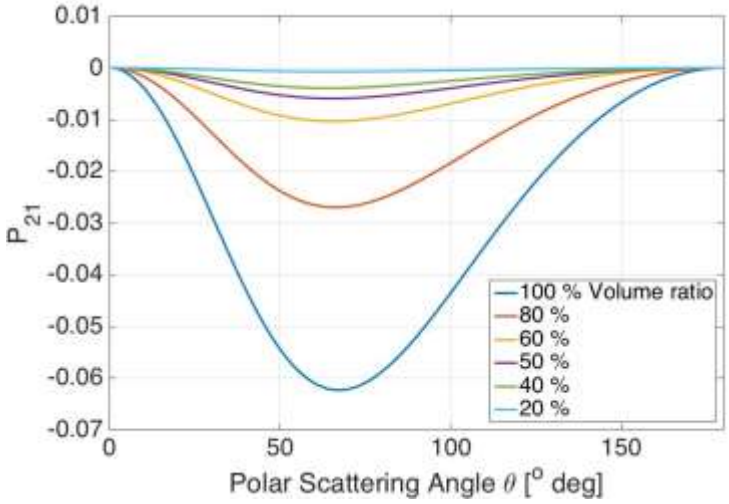

Fig. 10b. Influence of particle density on the phase matrix element P_{21} for a snow particle with 1 mm size at 270K and illuminated by 190 GHz microwave radiation.

As is evident from Fig. 10a, the high aspect ratio of the snowflake model leads to a dramatic decrease of the influence of the particle mass density on the phase function in the microwave region and for the BRM model. This is in contrast to the BRM graupel model studied by Tang et al., (2017), which has an aspect ratio much closer to one. Furthermore, the change in the phase function does not seem to be a unique function of the mass density alone. When looking at other phase matrix elements as in Fig. 10b, however, the results indicate a strong influence of the mass density on the polarization with a unique trend. In addition, the strongest gradient of the polarization elements as functions of the particle volume ratio exist between 100 and 60 percent.

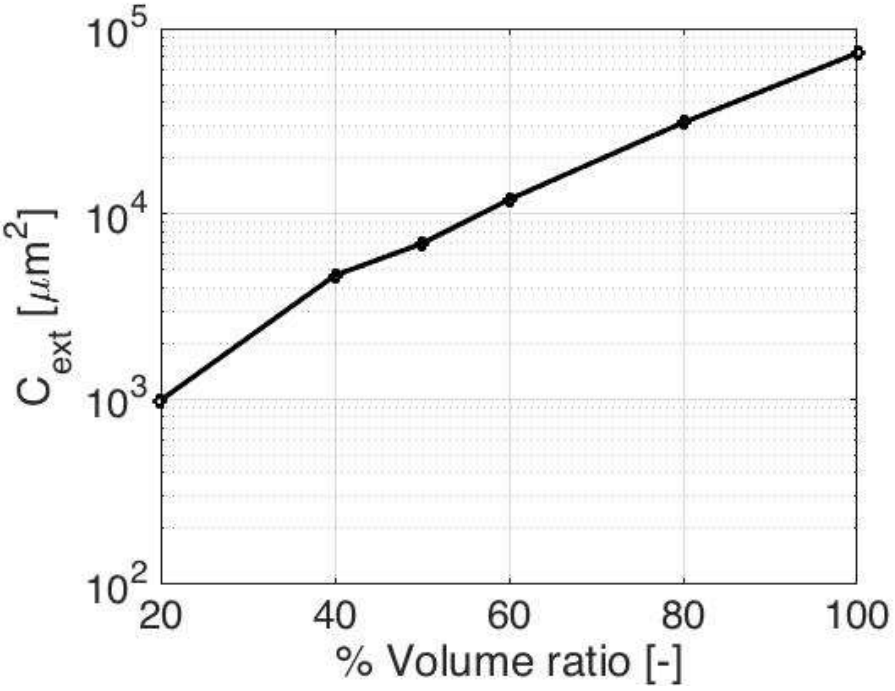

Fig. 11a. Influence of particle density on the extinction cross-section for a snow particle with 1 mm size at 270K and illuminated by 190 GHz microwave radiation.

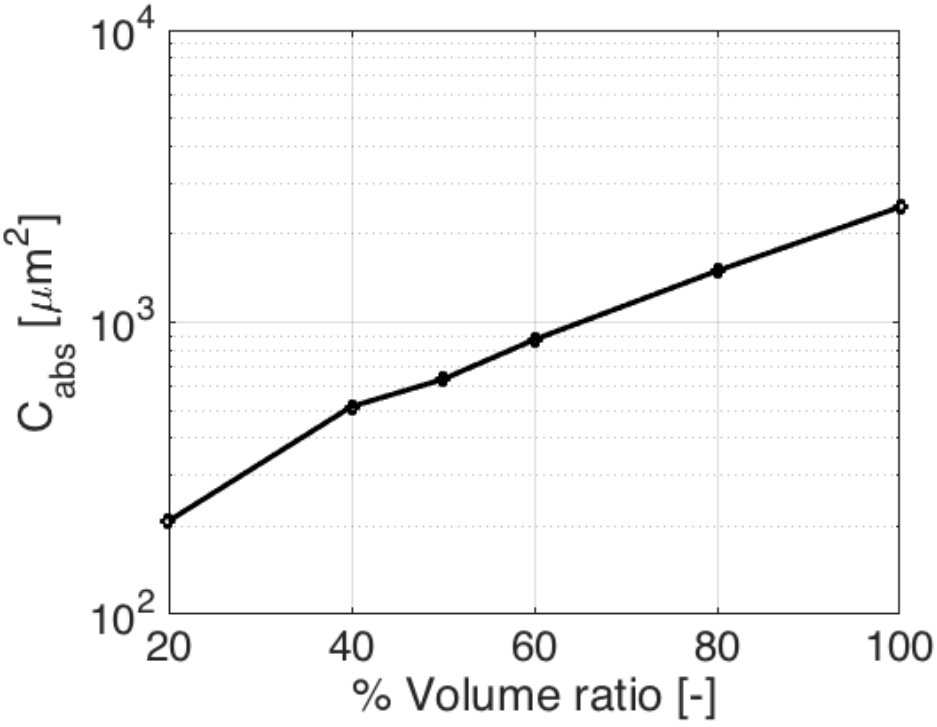

Fig. 11b. Influence of particle density on the absorption cross-section for a snow particle with 1 mm size at 270K and illuminated by 190 GHz microwave radiation.

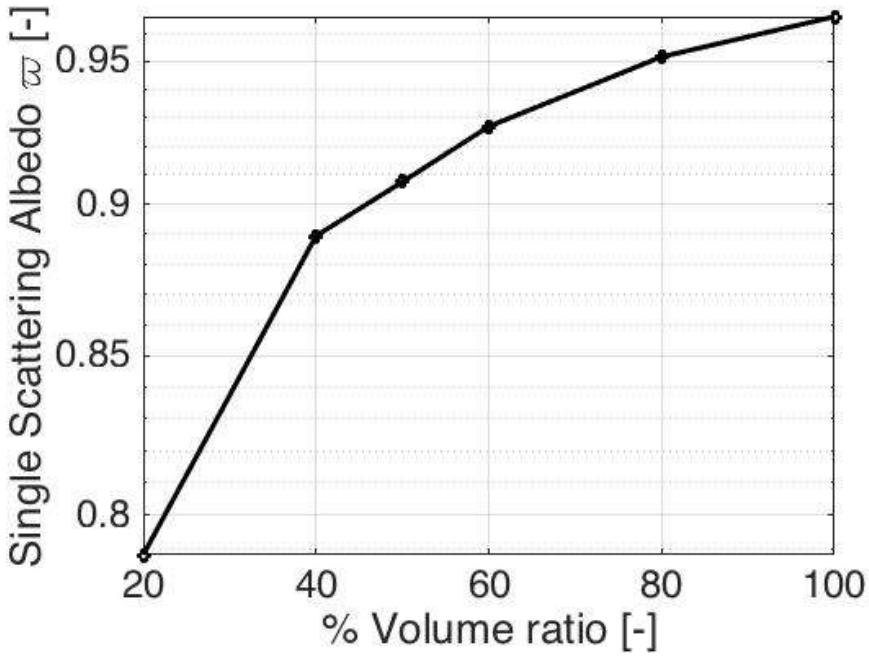

Fig. 11c. Influence of particle density on the single-scattering albedo for a snow particle with 1 mm size at 270K and illuminated by 190 GHz microwave radiation.

change in particle volume ratio, polarization and extinction on the other hand show a strong sensitivity.

The sensitivity of the single-scattering albedo towards the particle volume ratio is shown in Fig. and is also quite pronounced, albeit not at an exponential rate. Fig. 11c shows that the particle albedo diminishes from 0.96 towards a value below 0.85, i.e. an increased contribution of absorption to the total extinction of a particle at lower densities.

As a consequence, the single-scattering properties for the snow model particles as an input of the CRTM scattering coefficients have been computed at a volume fraction of $f_V = 0.2,\ 0.4, \mathit{and}\ 0.8$ in order to limit the parameter space that has to be swept by the computationally expensive FDTD computations. Constructing a database for the full parameter space consisting of the scattering particle Mie size parameter, temperature, density, mean wave number, and gamma distribution shape parameter Λ_g is beyond the scope of this study, which is explicitly focused on providing a more faithful representation of the microwave scattering properties of solid hydrometeors in the CRTM.

The relationship of the single-scattering properties of a BRM model particle and effective medium approaches such as the one by Bruggeman, (1935) or Maxwell Garnett, (1904) have already been discussed at length in the preceding study by Tang et al., (2017) and will consequently not be repeated here. The BRM parameters given in Fig. 5 and selected for the CRTM database calculations are adjusted such that the resulting particles cannot be considered “well mixed” in the sense of Tang et al., (2017) and the effective medium approximations will break down.

4. Computation of Bulk Scattering Properties

Based on the single-scattering properties that are computed following the tests discussed in the preceding section, the bulk scattering properties of the BRM snow and graupel models are computed along the lines of the procedures outlined in Baum

et al., (2007) and Wendisch and Yang, (2012), i.e. the bulk scattering properties are computed as a number size distribution-weighted average of the single-scattering properties. In particular, from Baum et al., (2007) the Eqs. (2)-(10) in Section 3 have been applied and the bulk phase function is normalized by the bulk extinction coefficient. The integrals that need to be evaluated in this process are computed using the simple trapezoidal quadrature rule, which, in part due to its robustness, is commonly used for this particular application. Especially for exponential- and Gamma size distributions the Gauss-Laguerre quadrature (see Elhay and Kautsky, 1987) provides an alternative to the trapezoidal rule via a simple variable substitution, however, this possibility has not been considered in this study. The necessary number density (number of particles per volume of air per particle size bin) for snow particles is given as an exponential distribution in Eq. (8), based on the results of Braham, (1990) and also discussed in relation to other size distributions by Petty and Huang, (2011). This is in contrast to the gamma distribution usually assumed for ice particles.

$$n_g\left(D_g\right) = N_{0g} \times \exp\left(-\Lambda_g D_g\right) \tag{8}$$

Using the notation of Petty and Huang, (2011), D_g is the geometric diameter of the individual scattering particle in the number density $n_g\left(D_g\right)$, which is identical to $D_{\max}$ in the present study, and the remaining parameters take on the following values:

$$\begin{aligned} N_{0g} &= 7.19 \times 10^{6}\, m^{-4} \\ \Lambda_g &= 1480\, m^{-1} \end{aligned} \tag{9}$$

As with the CRTM frequencies given in Table 2, the effective scattering particle sizes that need to be considered are essentially fixed by the CRTM ***CloudCoeff_type*** data structure. For the convenience of the reader, and as these data are as of yet unpublished, the effective sizes for solid hydrometeors available in the CRTM Release 2.1.3 are given in Table 3. It should be emphasized that in the CRTM Release 2.1.3 the effective size grid listed in Table 3 is the same for all hydrometeor classes listed in Table 1, irrespective of their density. This is of course undesirable in light of the density variation with particle size, but a fixed part of the current CRTM implementation. In order to achieve different effective particle sizes for snow, the exponent Λ_g of Eq. (8) needs to be adjusted. The Λ_g value corresponding to each CRTM effective size is given in the second column of Table 3.

The values of Λ_g listed in Table 3 have been computed by inverting the relationship between D_{eff} and Λ_g as given by e.g. Eq. (4) of Baum et al., (2007). A graphic plot of the functional relationship is shown in Fig. 12.

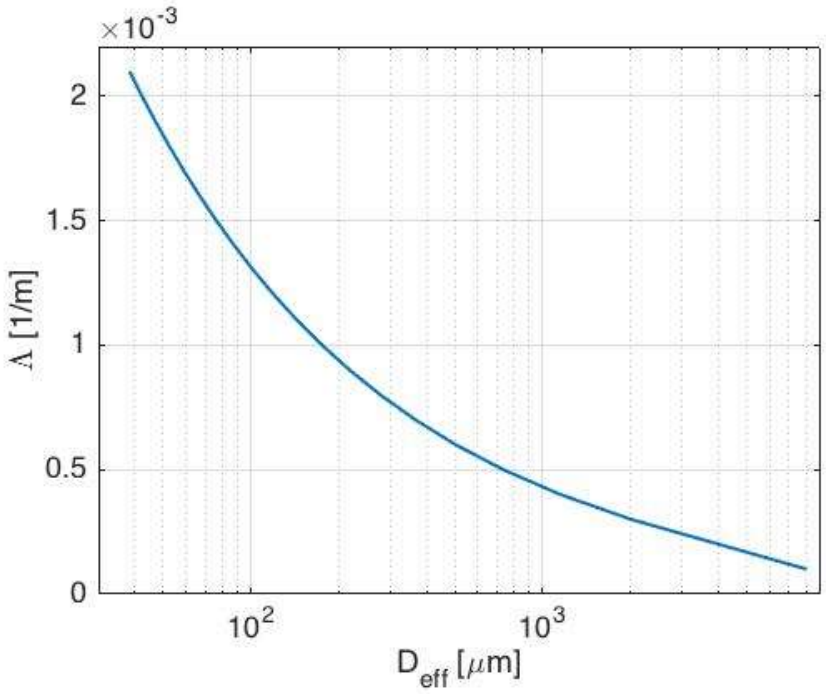

Fig. 12. Inverted relationship between D_{eff} and Λ_g as given by e.g. Eq. (4) of Baum et al., (2007). .

A sample result of a bulk phase function computed in this manner is shown in Fig. 13, together with a selection of the underlying phase functions for specific particle sizes in the background. The calculation results have been performed for T = 270K, 190 GHz, 40 percent volume fraction of ice, and an effective size of 1.5mm. As already discussed in section 3.1, a large part of the scattering properties of the snow and graupel particles in the microwave spectrum covered by the CRTM is either in or close the Rayleigh scattering regime, which is again evident in Fig. 13. As a probability distribution function by nature, the correct normalization of the phase function also needs to be ensured.

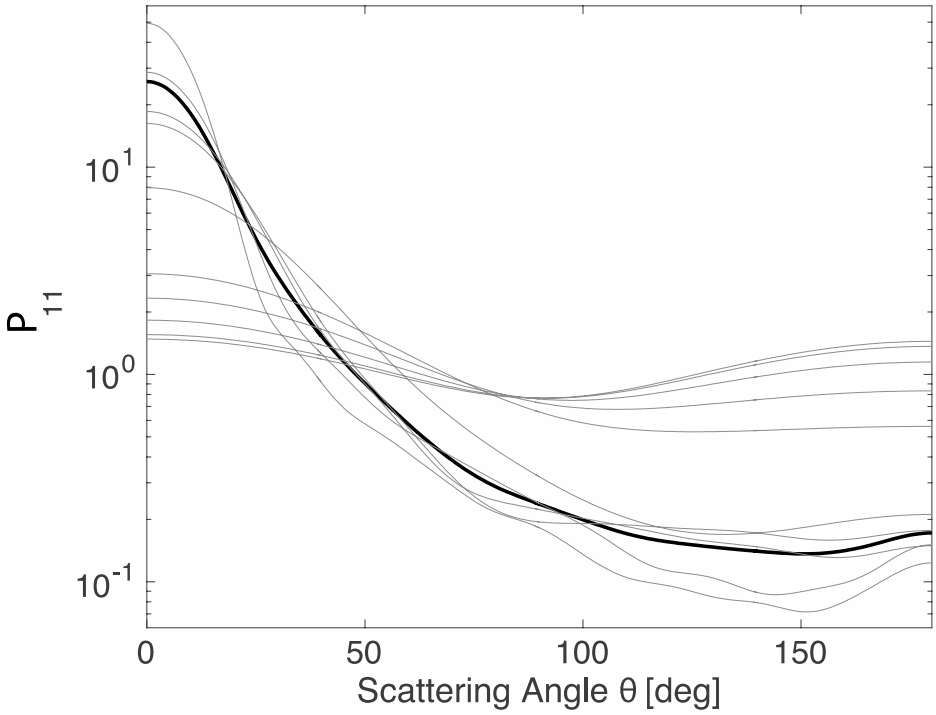

Fig. 13. Bulk phase function (black) of snow particles at T = 270K, 190 GHz, 40 percent volume fraction of ice, and an effective size of 2 mm. A selection of underlying single-particle phase functions is shown in gray.

As a consequence of the very specific primary application purpose of the CRTM in satellite data assimilation, several necessary design choices have been made during the development process of this library in order to realize a radiative transfer solver, that minimizes its associated computational burden while still retaining a maximum of physical accuracy in its results. This is in contrast to other general-purpose radiative transfer suites, such as e.g. ARTS by Eriksson et al., (2011) or, to a lesser degree, libRadtran by Emde et al., (2016), where a broad range of possible numerical methods is included such that the user can choose amongst the spectrum of available solvers to find an optimal compromise between accuracy and speed. As detailed in van Delst, (2013A), the CRTM not only includes a forward solver capability, but also Fortran 95 modules for Tangent-linear- , Adjoint- , and K-Matrix calculations.

Some of the design choices made during the development of the CRTM in order to optimize for computational speed also have certain indirect benefits for the user. Instrument data, especially for satellite based sensors, is handled internally by the CRTM, thus freeing the user of the responsibility to perform a convolution of the raw radiative transfer result with the instrument response function. Furthermore, while Fortran has been selected as the implementation language for speed, the consequent adherence to a modular programming style and the introduction of as many object oriented programming elements as allowed by the Fortran 2003 standard make the CRTM library source code itself a valuable addition to its existing documentation. A choice that introduces problems on the other hand is connected to scattering data input/output (I/O). Generally, performance benchmarks, such as the one by Michalakes, (2010) indicate that reading and writing data from or to file is significantly faster, if an unformatted binary file is used instead of a self-describing format like netCDF or HDF5. This, however, comes at the cost of losing the human-readability of the content of the binary data file and it can only be retrieved by writing a custom Fortran application using the inquiry subroutines shipped with the CRTM library modules.

Consequently, debugging the scattering LUT files of the CRTM is a difficult task. A number of errors associated with this design choice and uncovered during the improvement process will be discussed further below.

Scattering properties such as the extinction coefficient and the single-scattering albedo can be written to the CRTM CloudCoeff LUT file without further modification. The bulk phase function, however, needs to be projected onto a basis of Legendre polynomials, as the CRTM requires the phase function to be stored as the coefficients of the Legendre polynomial expansion. This is the case with many numerical solvers of the radiative transfer equation (RTE) and following the notation of Wendisch and Yang, (2012), the reconstruction of the phase function P_{11} in terms of Legendre polynomials $L_n(x)$ over the cosine of the polar scattering angle $\cos(\theta) \in [-1;1]$ and the corresponding expansion coefficients C_n is given in Eq. (10).

$$P_{11}(\cos(\theta)) = \sum_{n=0}^{\infty} C_n \times L_n(\cos(\theta)) \qquad (10)$$

Due to the low size parameter range of the snow and graupel particles in the microwave regime, their associated phase functions do not exhibit a pronounced forward diffraction peak. Instead, as can be seen in Fig. 13, the phase functions follow a rather smooth distribution. Consequently, the expansion in Eq. (10) can be applied directly and no special treatment of the forward peak, such as the δ-scaling by Joseph et al., (1976) and Zdunkowski, (2007) is necessary. Utilizing the orthogonality properties of the Legendre polynomials, the expression for the sought-after expansion coefficients is given in Eq. (11), following the conventions of Wendisch and Yang, (2012).

$$C_n = \frac{2n+1}{2} \int_{-1}^{+1} \left[P_{11}(\cos(\theta)) \times L_n(\cos(\theta)) \right] d\cos(\theta) \qquad (11)$$

The integral in Eq. (11) is evaluated using the QAG numerical integration routine from the QUADPACK library by Piessens et al., (1983). Both Eq. (10) and (11) are well known, but they are repeated here to clarify the notation used in the following paragraphs. A sample distribution of the absolute value of the newly computed expansion coefficients over the corresponding order of the Legendre polynomial is given in Fig. 14 for a test case at T = 160 K, 40 percent volume ratio, 24 GHz and 50 mm effective size. As shown in Fig. 14, the magnitude of the newly computed coefficients quickly decays to values of 10^{-4} and below for Legendre polynomials of order 15 and higher, such that only the first few orders of the expansion play a significant role in the reconstruction of the phase function. The computed coefficients are written to the CRTM CloudCoeff LUT files.

Using Eq. (10) however, one can also reconstruct the phase functions included in the default coefficient files of the CRTM release 2.1.3, leading to the aforementioned errors. This reveals numerous issues with the default scattering coefficients for solid hydrometeors. As a test case, the lowest size parameter for snow in the CRTM is selected, i.e. an effective size of 5 mm and an incident frequency of 1.4 GHz (see Tables 2 and 4) and the resulting coefficients are shown in Fig. 15. Consequently, the reconstructed phase function should lie in the Rayleigh regime with an anisotropy factor close or equal to g = 0. However, the reconstructed phase function shown in Fig. 16 bears no resemblance to a Rayleigh phase function and additionally takes on negative values over large sections of the polar scattering angle.

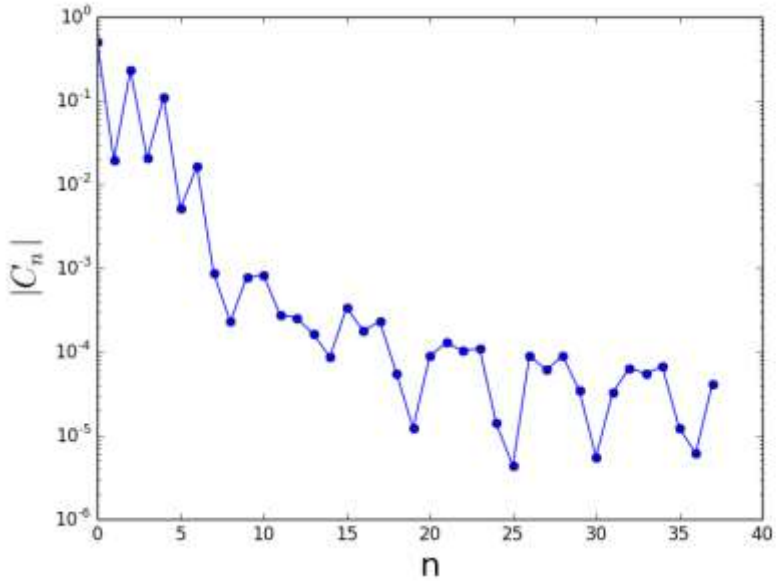

Fig. 14. Absolute value of Legendre expansion coefficients over expansion order n for a snow test case with T = 160 K, 40 percent volume ratio, 24 GHz and 50 μm effective size.

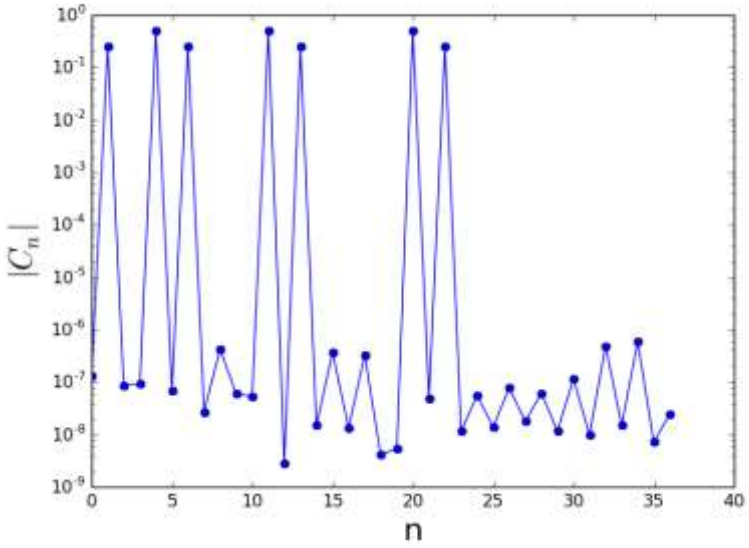

Fig. 15. Absolute value of **default CRTM Release 2.1.3** Legendre expansion coefficients over expansion order n for a snow test case at 1.4 GHz and 5 μm effective size. Note the non-vanishing coefficients at orders up to 20 for a phase function in the Rayleigh regime.

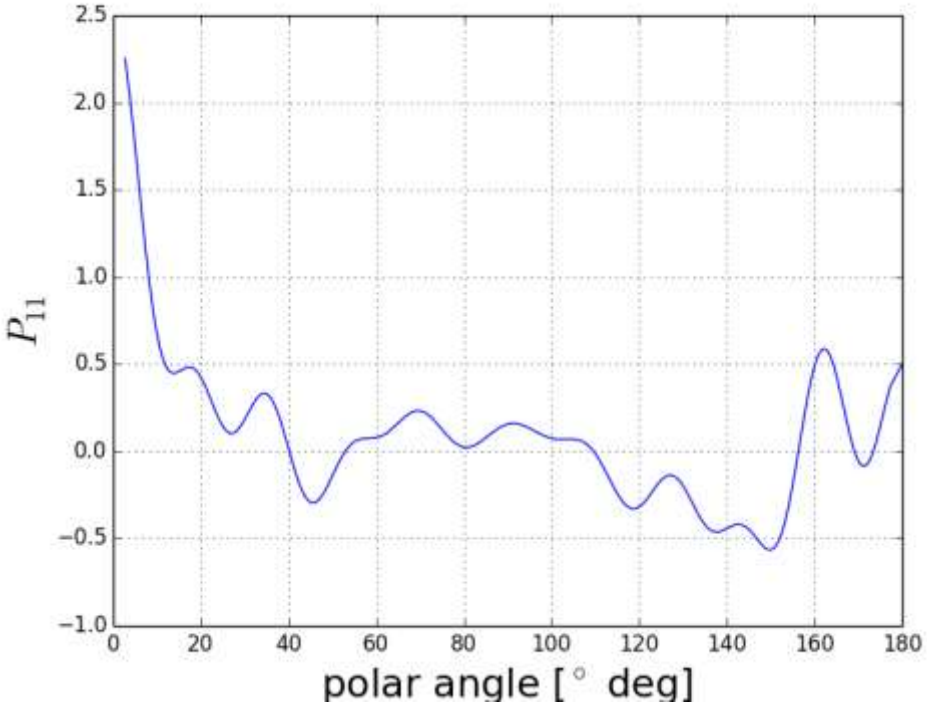

Fig. 16. Phase function reconstructed from the set of expansion coefficients shown in Fig. 14. Note the large sections of the polar scattering angle over which the phase function takes on negative values.

The reasons for this can be found in the corresponding Legendre expansion coefficients shown in Fig. 15. For the CRTM microwave scattering coefficients, the number of Legendre expansion terms is fixed at 36 for all sizes and frequencies. Instead of decreasing, the coefficients remain at high values up to expansion orders of n = 20. Other sets of default CRTM scattering coefficients show identical problems. This also contradicts the initial statement that the default CRTM coefficients are based on Mie calculations from Simmer, (1994). For comparison, a set of Legendre expansion coefficients computed from a Mie phase function for 1.4 GHz, $n_{ice} = 1.7838 + i \times 0.00416$ and 5 micrometers diameter is shown in Fig. 17. The original phase function has again been computed using Mieplot and the distribution of coefficients shown in Fig. 17 gives an indication as to how the Legendre expansion coefficients in the CRTM should actually behave. This is in stark contrast to the factual distribution shown in Fig. 15, leading to the unphysical phase function of Fig. 16, and not the expected Rayleigh phase function.

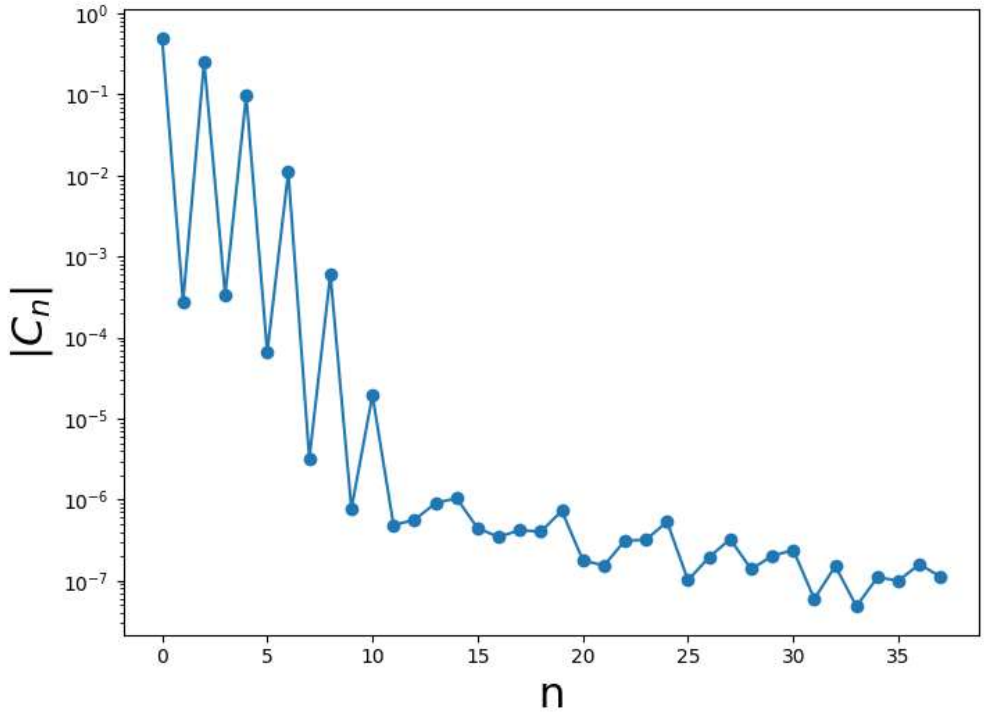

Fig. 17. Absolute value of Legendre expansion coefficients over expansion order n for a Mie test case at 1.4 GHz and 5 mm diameter. The reconstructed phase function is a Rayleigh phase function. Note the contrast to the factual CRTM distribution shown in Fig. 15.

Possible explanations for these issues are a too early truncation of the Legendre expansion, such that higher order terms cannot cancel out oscillations resulting from lower order contributions, and a quadrature of Eq. (11), which has been carried out with insufficient accuracy. In the Rayleigh-regime, the first explanation can be ruled out. It may also be admissible to truncate the expansion in Eq. (10) prematurely, in order to reduce the computational cost of the expansion, as long as the value of the truncated expansion at the quadrature points still agree with the original phase function within a given accuracy. However, this is again not the case for the phase function shown in Fig. 15, which bears no resemblance to a Rayleigh phase function. The case documented here has been randomly selected, as it is an obvious case of data corruption, however, this type of corruption of the phase functions occurs in all CRTM microwave scattering coefficients, i.e. for all sizes and frequencies, with the exception of the recently modified ice scattering coefficients based on MODIS Collection 6 data. Scattering properties other than the Legendre expansion coefficients bear no obvious flaws, however, issues with these are hard to detect, as the original source of the scattering properties is unknown.

5. Impact on the CRTM Radiative Transfer Computations

5.1. Single-column, Single cloud-layer test case

As simple test case for the new coefficients the AMSU-A Channel 15 radiance are computed as a function of the sensor zenith angle. The test case setup consists of a single one-dimensional pixel with the CRTM default ocean ground model and a single snow cloud of cloud optical thickness 0.7 and 0 for comparison with a clear sky calculation. Details of the implementation of the ocean model are given by van Delst, (2013A). Results are shown in Fig. 18a, comparing the pure

emission case with scattering by a snow cloud at 800 mbar pressure level. Water vapor, carbon dioxide, temperature, and pressure profile are taken from the US Standard Atmosphere. For the scattering calculations, the CRTM maximum resolution of 16 streams have been used. It can be seen in Fig. 18a that scattering reduces the radiance emitted from the ground and that there are slight differences in the angular distribution of the radiance between the default snow coefficients and the BRM coefficients with 20% volume ratio. Overall, the default coefficients have a lower radiance for higher sensor zenith angles. Of interest is also the small kink in the radiance close to zero degrees, which is likely an artifact of the CRTM scattering solver, as it occurs independently of the scattering coefficients but not for the pure emission solver (red). Figure 18b shows the relative difference between default and BRM radiances for the same setup as in Fig. 18a. The graph shows that the difference is less than -5% around nadir, crosses identity at around 23 degrees and then increases steadily up to a substantial 25% at near grazing sensor angles.

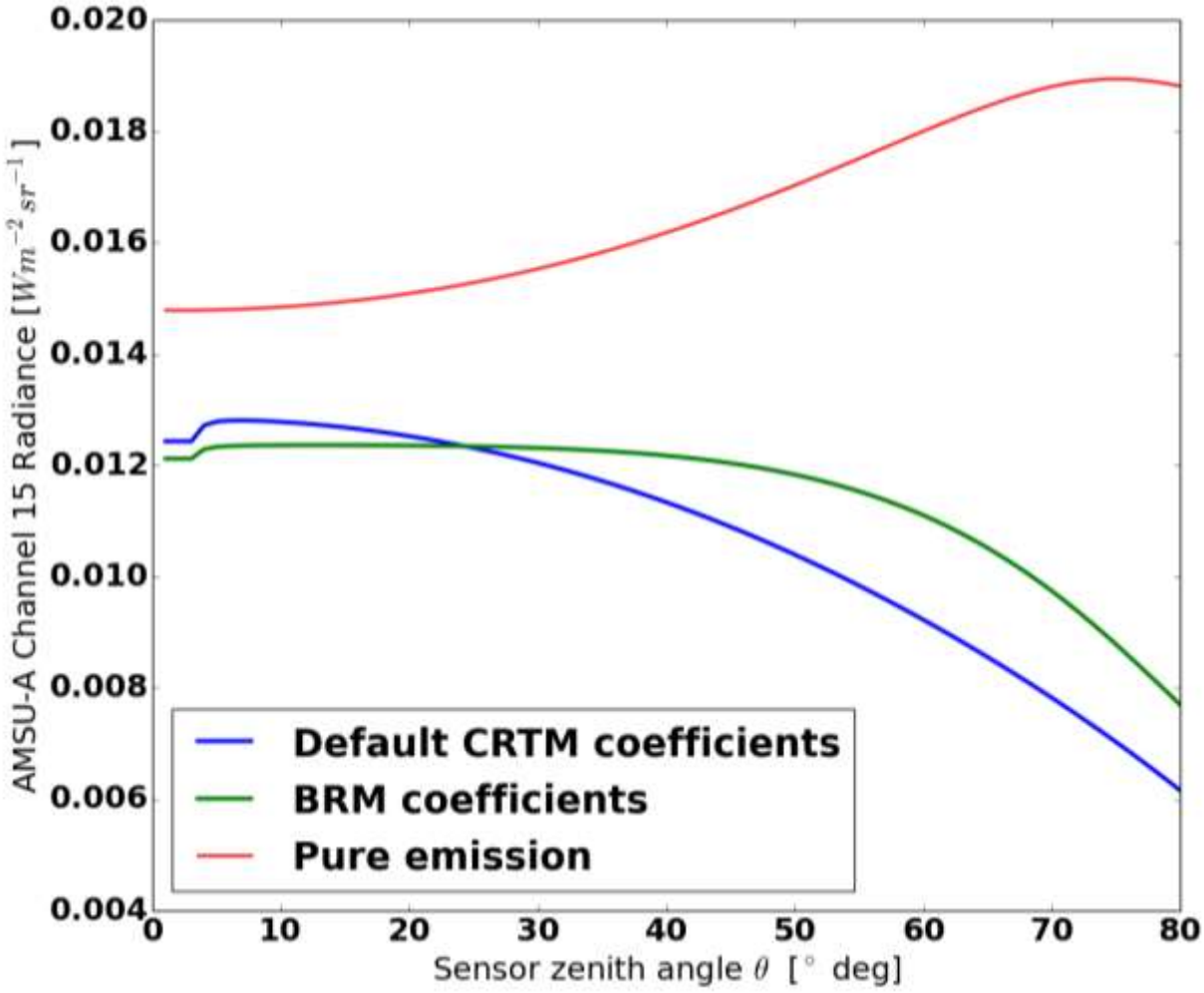

Fig. 18a. Radiance of Channel 15 of the AMSU-A instrument onboard the Aqua satellite over the sensor zenith angle as computed by the CRTM REL 2.1.3 for a single atmospheric column with and without a single snow cloud layer.

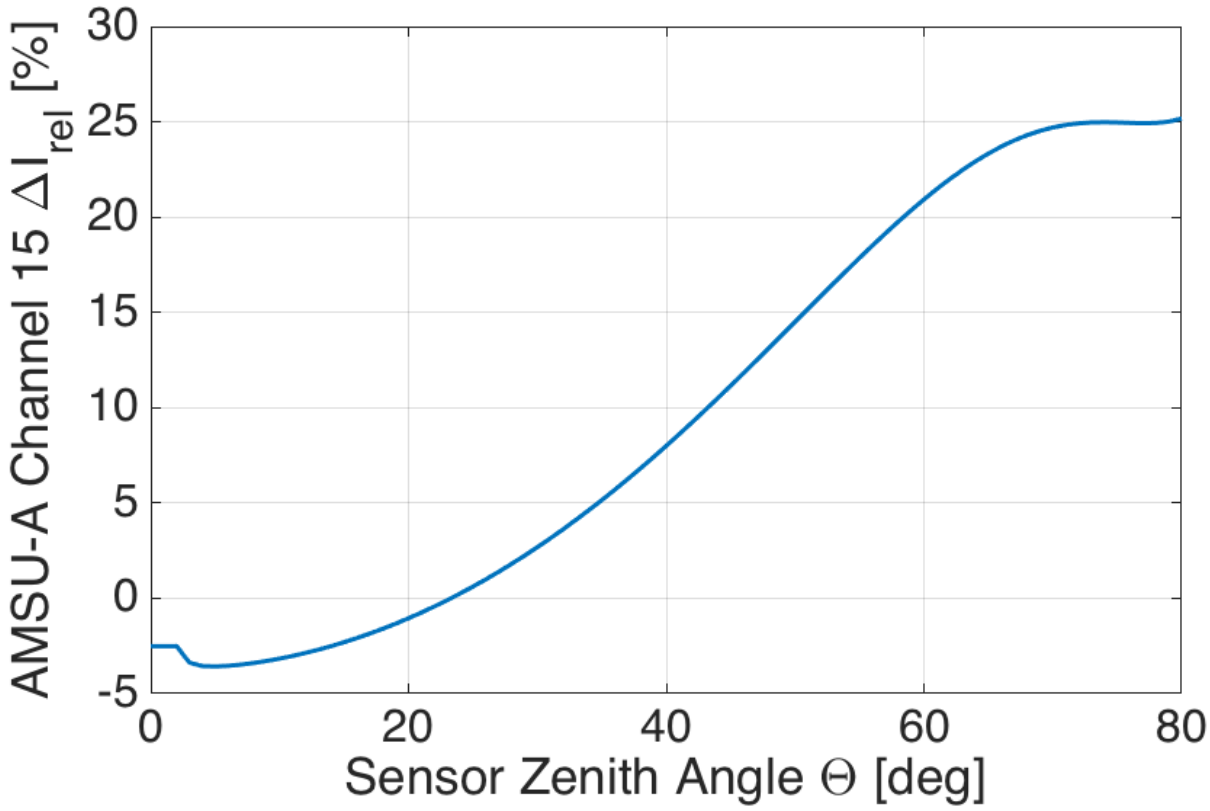

Fig. 18b. Relative difference of Aqua AMSU-A Ch. 15 radiance between default and BRM coefficients over the sensor zenith angle.

5.2. Satellite observations

In order to assess the impact of the density-variable microwave scattering properties on the CRTM radiative transfer calculations connected to satellite observations, the same test case as in Yi et al., (2016) has been chosen. The basis of this test case is the observational data of the AMSU-A microwave sounder aboard the Aqua satellite. This case offers the advantage of utilizing collocated data from other Aqua instruments, such as MODIS to complement the radiative transfer calculations. As a specific test case, a granule containing a large volume of ice clouds over the Indian Ocean has been chosen with a time stamp of 08:00 UTC 18 October 2013. An example of the instrument perspective and brightness temperatures (BTs) measured by AMSU-A, channel 15 for this particular granule are shown in Fig. 19. Figure 19 also shows a direct comparison between observed BTs and BTs computed using the default and BRM coefficients from left to right. Qualitatively, both sets of coefficients underestimate the BTs near the center line of the granule, and overestimate them near the eastern and western edges.

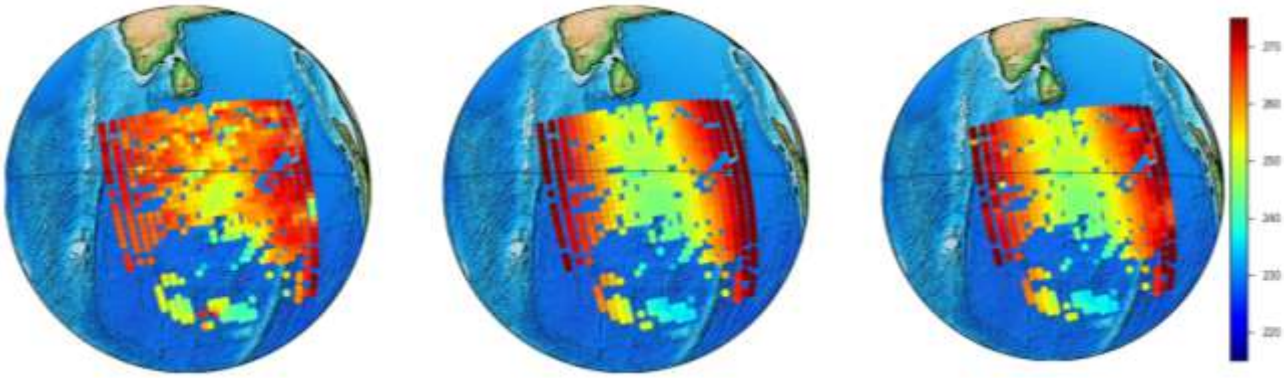

Fig. 19. Comparison of brightness temperature pixels in Kelvin of Channel 15 as observed by the AMSU-A instrument onboard the Aqua satellite (left), computed using the CRTM REL-2.1.3 default snow scattering coefficients (center), and computed using the BRM snow coefficients (right). Near-sided perspective projection at the 705 km altitude of the Aqua satellite orbit.

Cloud properties, such as cloud height and effective particle size are taken from operational collection 6 MODIS cloud retrievals, as shown in Fig. 20, and absorber concentrations, such as H_2O are extracted from MERRA reanalysis as an input of the CRTM radiative transfer calculations. Care needs to be taken, however, as MODIS products are available at a much higher resolution than AMSU-A data (e.g. 5 km versus 40km footprint size). BTs computed while utilizing MODIS data thus need to be averaged to the coarser AMSU-A resolution for comparison.

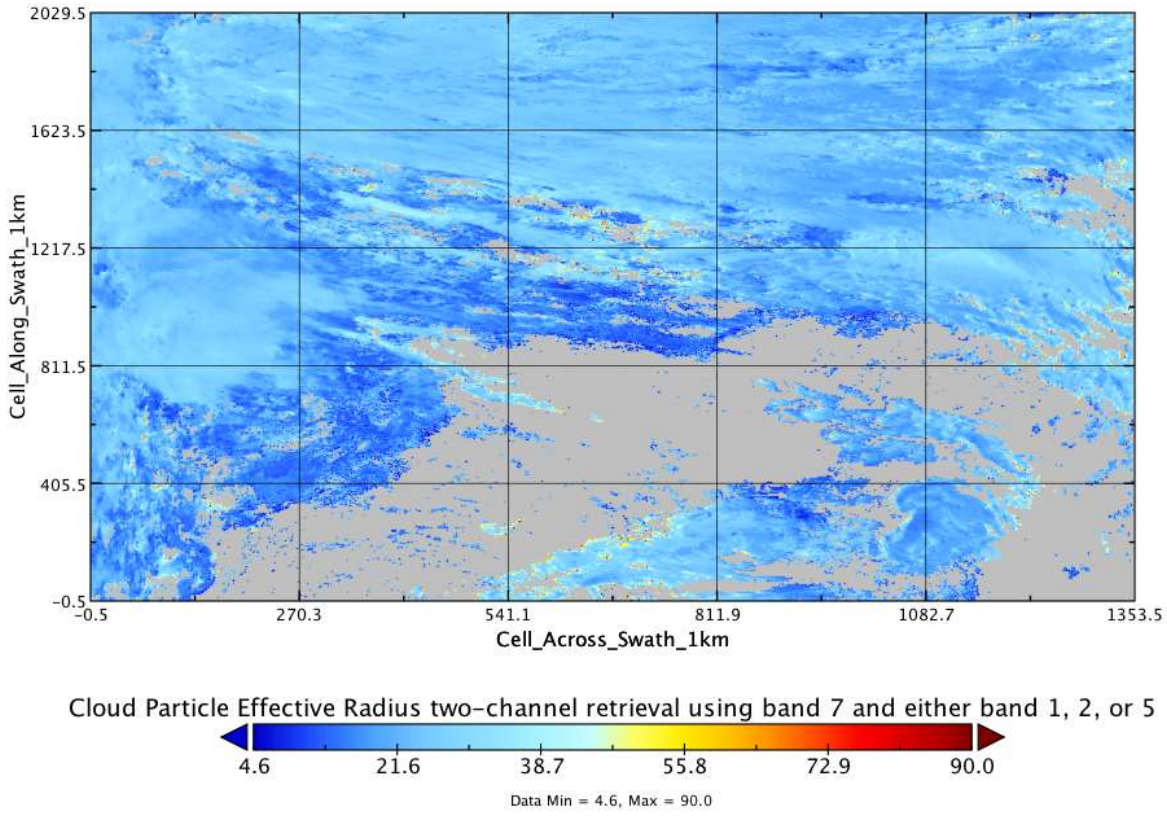

Fig. 20a. Retrieved Cloud Particle Effective Radius in micrometers from Aqua MODIS observations at 08:00 UTC 18 October 2013.

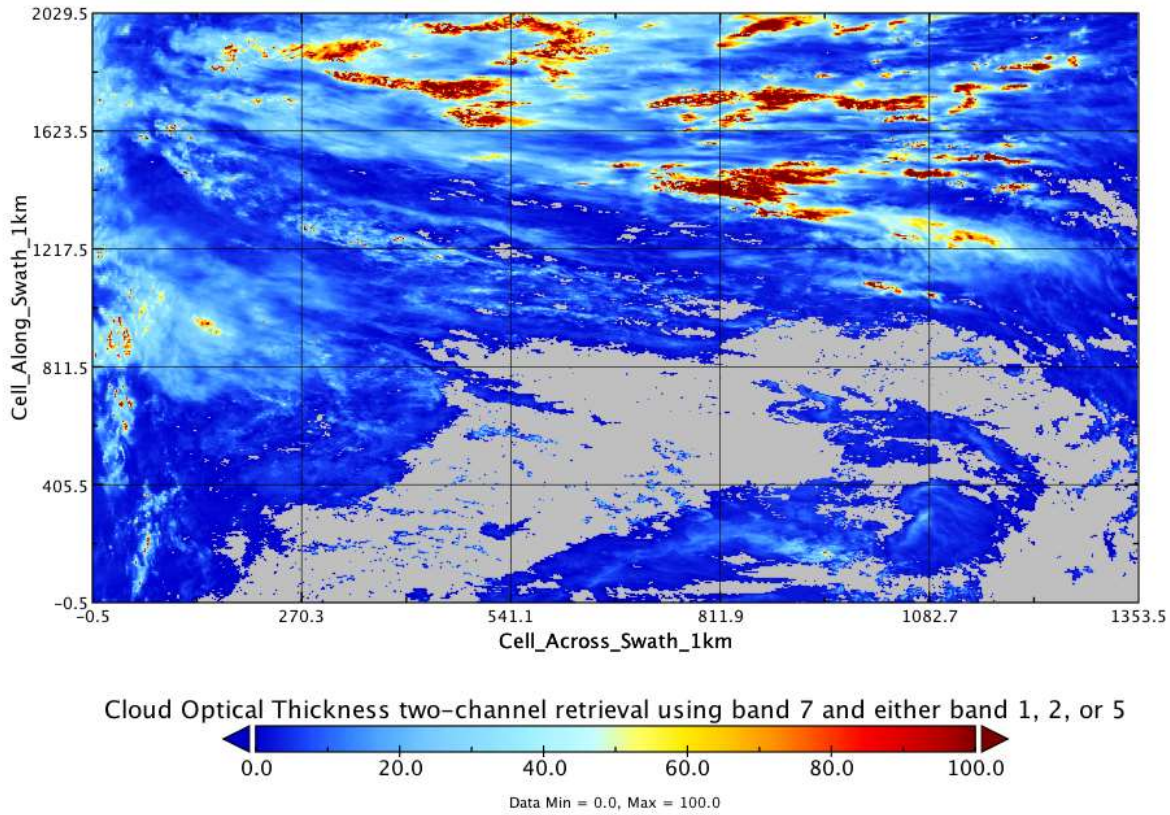

Fig. 20b. Retrieved Cloud Optical Thickness from Aqua MODIS observations at 08:00 UTC 18 October 2013.

For the calculations, only single layer ice cloud pixels have been selected, leading to a sample of 655 pixels in total. As all observed pixels are located over the Indian Ocean, the default ocean ground model implemented in the CRTM has been used for all calculations. As a full data satellite data assimilation study is beyond the scope of this project, the impact of the improved snow and graupel microwave coefficients will be assessed through sampling specific Aqua AMSU-A channels. Fig. 21 shows computed BT differences between measured and computed values for the selected Aqua granule as a function of cloud particle effective radius and cloud water path. The comparison has been performed for channels 7 and 8 (54.94 and 55.5 GHz), which are tropospheric temperature sounding channels.

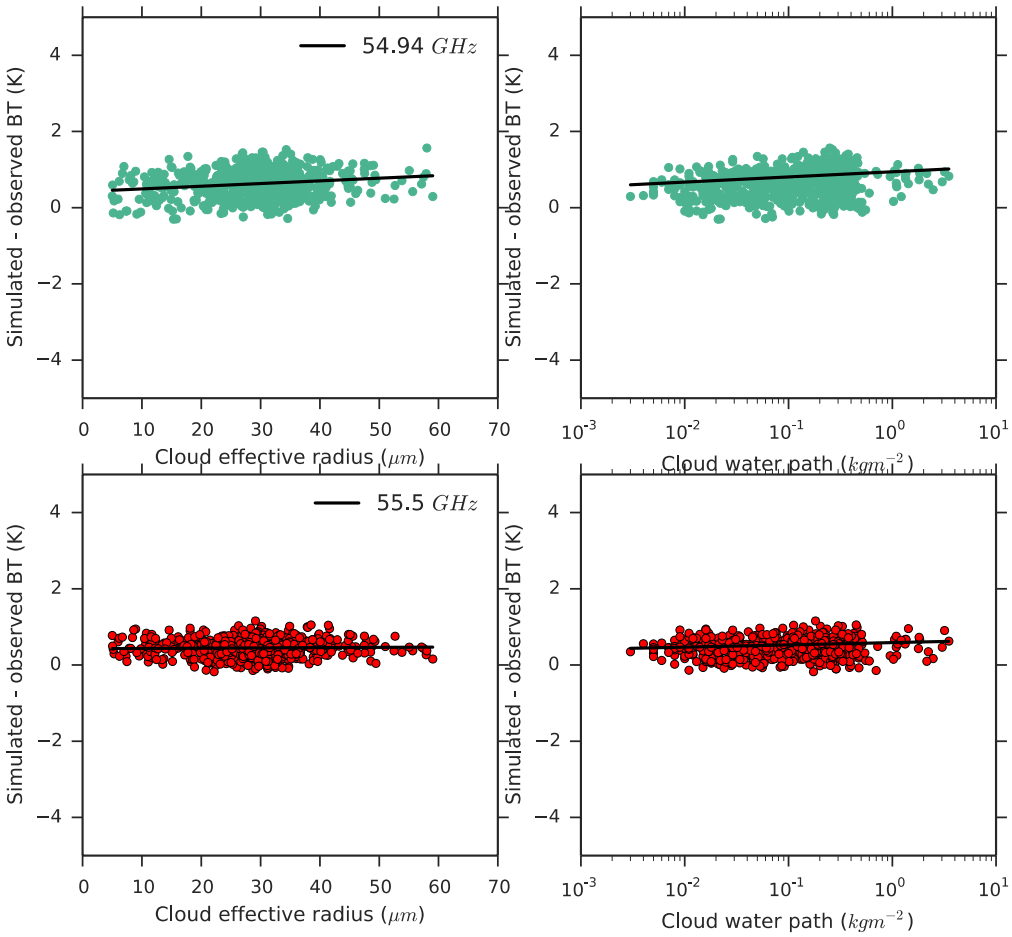

Fig. 21. Brightness temperature differences for AMSU-A channels 7 and 8 over cloud particle effective radius and cloud water path for the granule shown in Fig. 19. The linear regression of the sample pixels is shown in black.

Fig. 21 shows that for the selected set of channels, the BT differences are below 1 Kelvin and the linear regression of all the computed pixels is almost congruent to the abscissa, indicating excellent agreement between measured and computed values. Furthermore, this indicates that the newly computed coefficients do not negatively affect the values computed for the temperature sounding channels, i.e. this clear sky case is not affected by the newly computed scattering properties. As the cloud optical thickness for these two channels is almost negliable, the difference between the default and BRM coefficients is not appreciable and a direct comparison for this particular case and is thus not shown. At last, this also retroactively confirms the accuracy of the MERRA reanalysis data and the CRTM radiative transfer solver in this particular case.

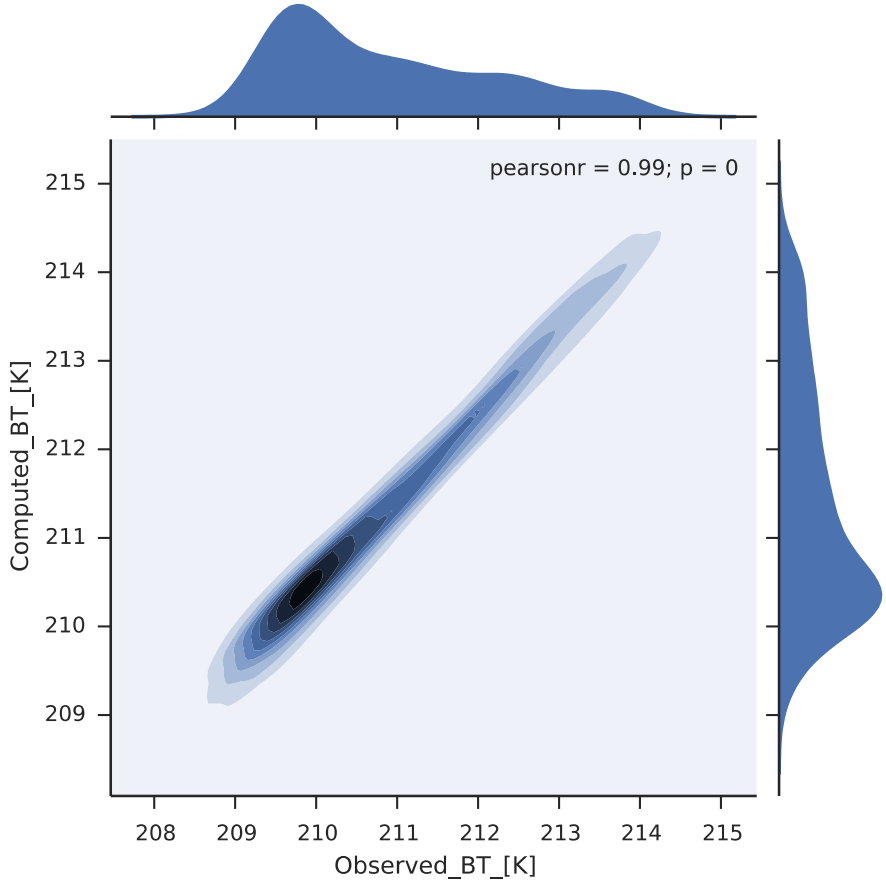

Fig. 22. Bivariate kernel density estimate of the measured and computed BTs for AMSU-A channel 8.

A direct comparison between the measured and computed BTs for Aqua AMSU-A channel 8 is shown in Fig. 22. Here, the bivariate kernel density estimate for the two random sets of brightness temperatures is clearly oriented along the diagonal and the correlation coefficient of the two distributions has a value 0.99, which is very close to one and again indicative of a strong positive correlation between observed and computed brightness temperatures while utilizing the improved coefficients. Finally, the channel 15 (89 GHz) results, which are used to retrieve information about cloud top height and cloud snow properties are scrutinized. As can be seen from Fig. 23, however, the computed BTs diverge significantly from the observed ones. Using a different set of scattering coefficients for the computations nevertheless always leads to similar results. Fig. 23 also shows the resulting histograms for the Default SNOW_CLOUD coefficients, as well as BRM SNOW_CLOUD coefficients for 20% and 40% volume ratio respectively. All three curves have a strong similarity and especially for lower BTs, the BRM SNOW_CLOUD coefficients are consistent with the results for the other two coefficient sets. However, the default coefficient results show the highest percentage of high temperature pixels, while the BRM results overall have lower BTs.

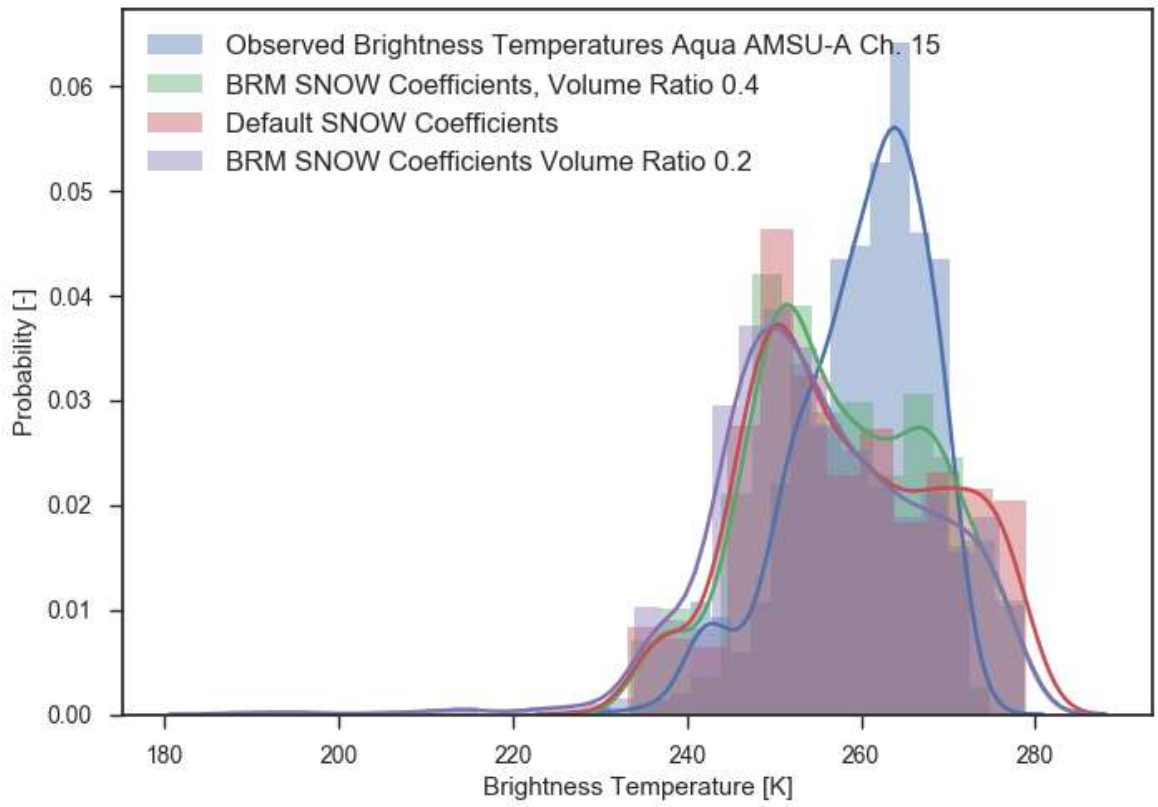

Fig. 23. Kernel density estimate of the AMSU-A Channel 15 (i.e. 89 Ghz) BTs in the observed (blue) and computed cases, assuming MODIS Collection 6 ICE_CLOUD, BRM SNOW_CLOUD, and default WATER_CLOUD optical properties respectively.

This is indicative of the fact that for the low size parameters in the observed microwave regime, the actual particle morphology plays a minor role in light scattering, as the single-scattering properties approach the Rayleigh regime. The consistency of the snow coefficients with the selected ice and water droplet results in Fig. 23 also suggests that the underlying cause for the disagreement between the measured and computed BTs is not related to the coefficients, but rather to the model setup, i.e. uncertainties in the retrieved MODIS cloud properties, a too constrained range of available effective particle sizes in the CRTM itself or unspecified issues with the ADA radiative transfer solver of the CRTM.

The mean BT value for the entire AMSU-A granule, however, is computed within an accuracy of less than 2 Kelvin, as $\langle T_B \rangle_{Obs} = 259.913616489$ and $\langle T_B \rangle_{Obs} = 258.033560153$.

Lastly, the sensitivity of the new set of snow coefficients for 40% volume ratio is tested with respect to perturbations in snow cloud properties, such as particle effective radius, ice water path, and cloud top pressure. The results are summarized in Table 5 and given for channels 1 and 15. As expected, the absolute mean difference in brightness temperature is much more sensitive to changes in cloud properties for channel 15 than for channel 1. For channel 15, a perturbation of the cloud top pressure has the most significant impact, with mean BT changes of the order of 1-2 Kelvin. Perturbation of the particle effective radius and ice water path induce changes of about 0.6 Kelvin in each case.

Table 5. Summary of mean BT changes in Kelvin, with respected to the unperturbed case for AMSU-A channels 1 and 15 using the BRM microwave scattering properties of snow.

Perturbation	**AMSU-A Ch. 1**	**AMSU-A Ch. 15**

particle effective radius	+5%	0.00910351	0.60322229
	-5%	-0.00910351	-0.60322229
Ice water path	+5%	-0.00910351	-0.60321893
	-5%	0.00910351	0.60322382
Cloud top pressure	+5%	0.4104681	2.3024516
	-5%	-0.40804611	-1.245671

6. Conclusion

In this paper, the bicontinuous leveled-wave model of Berk, (1987) has been applied to snow and graupel particles in order to compute their single-scattering properties in the microwave regime with an arbitrary mass density. These properties have been computed using the FDTD scattering code by Yang and Liou, (1996) and the convergence of the results has been thoroughly demonstrated. With these single-scattering properties cloud scattering coefficients for the CRTM have been extended as such and it is demonstrated that the existing coefficients in the default CRTM contain severe unphysical properties and that the new set of coefficients provide a necessary step forward towards a faithful representation of microwave scattering properties of solid hydrometeors in the CRTM. Case studies for the application of the new cloud coefficients were performed, demonstrating a significant variability of the microwave scattering properties of snow clouds under variation of the density.

Acknowledgements

This study was supported by NOAA Grant NA15NES4400003. A major portion of the calculations was carried out at the Texas A&M University Supercomputing Facilities, and the authors gratefully acknowledge the facility staff for their help and assistance. The corresponding author also acknowledges the very helpful comments of Dr. Maxim Yurkin regarding the DDA calculations included in this study.

References

Barrett, J. W., H. Garcke, R. Nürnberg (2012): Numerical computations of faceted pattern formation in snow crystal growth. Physical Review E 86, id 011604. doi:10.1103/PhysRevE.86.011604

Baum, B. A., P. Yang, A. J. Heymsfield, S. Platnick, M. D. King, Y.-X. Hu, amd S. T. Bedka (2005): Bulk scattering models for the remote sensing of ice clouds. Part II: Narrowband models. Journal of Applied Meteorology 44, pp. 1896-1911. Doi:10.1175/JAM2309.1.

Baum, B. A., P. Yang, S. Nasiri, A. K. Heidinger, A. J. Heymsfield, and J. Li (2007): Bulk Scattering Properties for the Remote Sensing of Ice Clouds. Part III: High-Resolution Spectral Models from 100 to 3250 cm^{-1}. Journal of Applied Meteorology and Climatology 46, pp. 423-434.

Berk, N. F. (1987): Scattering Properties of a Model Bicontinuous Structure with a Well Defined Length Scale. Physical Review Letters 58, pp. 2718-2721.

Berk, N. F. (1991): Scattering properties of the leveled-wave model of random morphologies. Physical Review A 44, pp. 5069-5079.

Bi, L., P. Yang, G. W. Kattawar, and M. I. Mishchenko (2013): Efficient implementation of the invariant imbedding T-Matrix method and the separation of variables method applied to large nonspherical inhomogeneous particles. Journal of Quantitative Spectroscopy and Radiative Transfer 116, pp. 169-183. doi:10.1016/j.jqsrt.2012.11.014

Bohren, C. F., and D. R. Huffman (1993): *Absorption and Scattering of Light by Small Particles*. Wiley, New York.

Braham, R. R., Jr. (1990): Snow particle size spectra in lake effect snows. Journal of Applied Meteorology 29, pp. 200-207.

Bruggeman, D. A. G. (1935): Berechnung verschiedener physikalischer Konstanten von heterogenen Substanzen: 1. Dielektrizitätskonstanten und Leitfähigkeiten der Mischkörper aus isotropen Substanzen. Annalen der Physik 5, pp. 636-664.

Cahn, J. W., and J. E. Hilliard (1958): Free energy of a nonuniform system. 1. Interfacial free energy. Journal of Chemical Physics 28, pp. 258.

Chen, S. H., and S. L. Chang (1991): Simulation of bicontinuous microemulsions: comparison of simulated real-space microstructures with scattering experiments. Journal of Applied Crystallography 24, pp. 721-731.

Chen, Y., F. Weng, Y. Han, and Q. Liu (2008): Validation of the Community Radiative Transfer Model by using CloudSat data. Journal of Geophysical Research 113, D00A03, doi:10.1029/2007JD009561.

Chew, W. C., and W. H. Weedon (1994): A 3D perfectly matched medium from modified Maxwell's equations with stretched coordinates. Microwave Optics Technical Letters 7, pp. 599-604.

Criscione, A., I. V. Roisman, S. Jakirlic, and C. Tropea (2015): Towards modelling of initial and final stages of supercooled water solidification. International Journal of Thermal Sciences 92, pp. 150-161. doi:10.1016/j.ijthermalsci.2015.01.021

van Delst, P. (2013A): CRTM: v2.1.3 User Guide. Joint Center for Satellite Data Assimilation. Available at http://ftp.emc.ncep.noaa.gov/jcsda/CRTM/REL-2.1.3/ (Retrieved July 5, 2017).

van Delst, P. (2013B): CRTM v2.1.3 source code. Available at http://ftp.emc.ncep.noaa.gov/jcsda/CRTM/REL-2.1.3/ (Retrieved July 5, 2017).

Ding, K.-H., X. Xu, and L. Tsang (2010): Electromagnetic Scattering by Bicontinuous Random Microstructures With Discrete Permittivities. IEEE Transactions on Geoscience and Remote Sensing 48, pp. 3139-3151.

Ding, S., P. Yang, F. Weng, Q. Liu, Y. Han, P. van Delst, J. Li, and B. Baum (2011): Validation of the community radiative transfer model. Journal of Quantitative Spectroscopy and Radiative Transfer 112, pp. 1050-1064.

Draine, B. T., and P. J. Flatau (1994): Discrete-dipole approximation for scattering calculations. Journal of the Optical Society of America A 11, pp. 1491-1499.

Elhay, S., and J. Kautsky (1987): Algorithm 655 IQPACK: FORTRAN Subroutines for the Weights of Interpolatory Quadratures. ACM Transactions on Mathematical Software 13, pp. 1200-0399.

Emde, C., R. Buras-Schnell, A. Kylling, B. Mayer, J. Gasteiger, U. Hamann, J. Kylling, B. Richter, C. Pause, T. Dowling, and L. Bugliaro (2016): The libRadtran software package for radiative transfer calculations (version 2.0.1). Geoscientific Model Development 9(5), pp. 1647-1672.

Eriksson, P., S. A. Buehler, C. P. Davis, C. Emde, and O. Lemke (2011): ARTS, the atmospheric radiative transfer simulator, version 2. Journal of Quantitative Spectroscopy and Radiative Transfer 112, pp. 1551-1558. doi:10.1016/j.jqsrt.2011.03.001.

Gravner, J., and D. Griffeath (2009): Modeling snow-crystal growth: A three-dimensional mesoscopic approach. Physcial Review E 79, id 011601.

Heidinger, A. K., C. O'Dell, R. Bennartz, and T. Greenwald(2006): The Successive-Order-of-Interaction Radiative Transfer Model. Part I: Model Development. J. Appl. Met. and Clim. 45, pp. 1388-1402.

Hiller, J. D., and H. Lipson (2009): STL 2.0: A Proposal for a Universal Multi-Material Additive Manufacturing File Format. Cornell University. Retrieved October 2nd, 2017.

Hong, S.-Y., J. Dudhia, and S.-H. Chen (2004): A Revised Approach to Ice Microphysical Processes for the Bulk Parameterization of Clouds and Precipitation. Monthly Weather Review 132, pp. 103-120.

Hu, M., H. Shao, D. Stark, K. Newman, C. Zhou, and X. Zhang (2016): Grid-point Statistical Interpolation (GSI) User's Guide Version 3.5. Developmental Testbed Center. Available at http://www.dtcenter.org/com-GSI/users/docs/index.php, 141 pp.

van de Hulst, H. C. (1981): Light Scattering by Small Particles. Dover Publications, Mineola NY.

Iwabuchi, H., and P. Yang (2011): Temperature dependence of ice optical constants: Implications for simulating the single-scattering properties of cold ice clouds. Journal of Quantitative Spectroscopy and Radiative Transfer 112, pp. 2520-2525.

Joseph, J., W. Wiscombe, and J. Weinman (1976): The Delta-Eddington approximation for radiative flux transfer. Journal of Atmospheric Sciences 33, pp. 2452-2459.

Kahnert, M. (2005): Irreducible representations of finite groups in the T-Matrix formulation of the electromagnetic scattering problem. Journal of the Optical Society of America A 22, pp. 1187-1199.

Kalnay, E. (2003): Atmospheric Modeling, Data Assimilation and Predictability. Cambridge University Press.

Kikuchi, K., T. Kameda, K. Higuchi, A. Yamashita, and Working group members for new classification of snow crystals (2013): A global classification of snow crystals, ice crystals, and solid precipitation based on observations from middle latitudes to polar regions. Atmospheric Research 132, pp. 460-472.

Laven, P. (2003): Simulation of rainbows, coronas, and glories by use of Mie theory. Applied Optics 42, pp. 436-444.

Liu, Q., and F. Weng (2006): Advanced Doubling-Adding Method for Radiative Transfer in Planetary Atmospheres. J. Atm. Sci. 63, pp. 3459-3465.

Macke, A., J. Müller, and E. Raschke (1996): Single scattering properties of atmospheric ice crystals. Journal of Atmospheric Science 53, pp. 2813-2203.

Marsaglia, G., and W. W. Tsang (2000): A Simple Method for Generating Gamma Variables. ACM Transactions on Mathematical Software 26, pp. 363-372.

Marsaglia, G. (2003): Xorshift RNGs. Journal of Statistical Software 8, (14).

Maxwell Garnett, J. C. (1904): Colours in Metal Glasses and in Metallic Films. Proceedings of the Royal Society 203, pp. 385-420.

McCumber, M., W.-K. Tao, and J. Simpson (1991): Comparison of Ice-Phase Microphysical Parameterization Schemes Using Numerical Simulations of Tropical Convection. Journal of Applied Meteorology 30, pp. 985-1004.

Michalakes, J. G. (2002): Technical Report: Preliminary I/O Performance in WRF: NetCDF vs. Binary with Quilt I/O. available at: http://wrf-model.org/PRESENTATIONS/IO/WRF_IO_test.htm (Retrieved on July 3, 2017).

Mie, G. (1908): Beiträge zur Optik trüber Medien, speziell kolloidaler Metallösungen. Annalen der Physik 4. Folge, Band 25, pp. 377-445, doi:10.1002/andp.19123441102.

Mishchenko, M. I., J. W. Hovenier, and L. D. Travis (2000): Light Scattering by Nonspherical Particles: Theory, Measurements, and Applications. Academic Press San Diego, CL.

Osher, S., and J. A. Sethian (1988): Fronts propagating with curvature-dependent speed: Algorithms based on Hamilton-Jacobi formulations. Journal of Computational Physics 79, pp. 12-49. doi:10.1016/0021-9991(88)90002-2

Petty, G. W., and W. Huang (2011): The Modified Gamma Size Distribution Applied to Inhomogeneous and Nonspherical Particles: Key Relationships and Conversions. Journal of the Atmospheric Sciences 68, pp. 1460-1473.

Piessens, R., E. de Doncker-Kapenga, C. W. Überhuber, and D. Kahaner (1983): QUADPACK: A subroutine package for automatic integration. Springer-Verlag Berlin/Heidelberg.

Platnick, S., K. G. Meyer, M. D. King, G. Wind, N. Amarasinghe, B. Marchant, G. T. Arnold, Z. Zhang, P. A. Hubanks, R. E. Holz, P. Yang, W. L. Ridgway, and J. Riedi (2017): The MODIS Cloud Optical and Microphysical Products: Collection 6 Updates and Examples from Terra and Aqua. IEEE Transactions on Geoscience and Remote Sensing 55, pp. 502-524.

Pruppacher, H. R., and J. D. Klett (1978): Microphysics of Clouds & Precipitation. D. Reidel Publishing, Dordrecht, Holland.

Rodgers, C. D. (2000): Inverse Methods for Atmospheric Sounding: Theory and Practice. World Scientific, London, UK.

Sahimi, M. (2002): Heterogeneous Materials 1: Linear Transport and Optical Properties. Springer-Verlag New York.

Simmer, C. (1994): Satellitenfernerkundung Hydrologischer Parameter der Atmosphäre mit Mikrowellen. Verlag Dr. Kovac Hamburg

Stamnes, K., S.-C. Tsay, W. Wiscombe, and K. Jayaweera (1988): Numerically stable algorithm for discrete-ordinate-method radiative transfer in multiple scattering and emitting layered media. Applied Optics 27, pp. 2502-2509.

Stegmann, P. G., C. Tropea, E. Järvinen, M. Schnaiter (2016): Comparison of measured and computed phase functions of individual tropospheric ice crystals. Journal of Quantitative Spectroscopy and Radiative Transfer 178, pp. 379-389. doi:10.1016/j.jqsrt.2015.12.019

Tang, G., P. Yang, P. G. Stegmann, R. L. Panetta, L. Tsang, and B. Johnson (2017): Effect of particle shape, density, and inhomogeneity on the microwave optical properties of graupel and hailstones. Accepted for publication in IEEE Transactions on Geoscience and Remote Sensing.

Wang, P. K. (2002): Ice Microdynamics. Academic Press San Diego, CA.

Weiland, T. (1977): A Discretization Method for the Solution of Maxwell's Equations for Six-Component Fields. Electronics and Communications AEUE 31, pp. 116-120.

Weiland, T. (1984): On the Numerical Solution of Maxwell's Equations and Applications in the Field of Accelerator Physics. Particle Accelerators 15, pp. 245-292.

Wendisch, M., and P. Yang (2012): Theory of Atmospheric Radiative Transfer. Wiley-VCH Weinheim, Germany.

Weng, F., and Q. Liu (2003): Satellite Data Assimilation in Numerical Weather Prediction Models. Part 1: Forward Radiative Transfer and Jacobian Modeling in Cloudy Atmospheres. Journal of the Atmospherica Sciences 60, pp. 2633-2646.

Wood, N. B., T. L'Ecuyer, A. J. Heymsfield, G. L. Stephens, D. R. Hudak, and P. Rodriguez (2014): Estimating snow microphysical properties using collocated multisensory observations. Journal of Geophysical Research: Atmospheres 119, pp. 8941-8961. doi:10.1002/2013JD021303

Xiong, C., and J. Shi (2014): Simulating polarized light scattering in terrestrial snow based on bicontinuous random medium and Monte Carlo ray tracing. Journal of Quantitative Spectroscopy and Radiative Transfer 133, pp. 177-189. doi:10.1016/j.jqsrt.2013.07.026

Yang, P., and K. N. Liou (1995): Light scattering by hexagonal ice crystals: Comparison of finite-difference time domain and geometric optics models. Journal of the Optical Society A 12, pp. 162-176.

Yang, P., and K. N. Liou (1996): Finite-difference time domain method for light scattering by small ice crystals in three-dimensional space. Journal of the Optical Society of America A 13, pp. 2072-2085.

Yee, K. S. (1966): Numerical solution of initial boundary value problems involving Maxwell's equations in isotropic media. IEEE Transactions on Antennas and Propagation 14, pp. 302-307

Yi, B., P. Yang, Q. Liu, P. van Delst, S.-A. Boukabara, and F. Weng (2016): Improvements on the ice cloud modeling capabilities of the Community Radiative Transfer Model. Jounral of Geophysical Research: Atmospheres 121. doi:10.1002/2016JD025207

Yurkin, M. A., V. P. Maltsev, and A. G. Hoekstra (2007): The discrete dipole approximation for simulation of light scattering by particles much larger than the wavelength. Journal of Quantitative Spectroscopy and Radiative Transfer 106, pp. 546-557.

Zdunkowski, W., T. Trautmann, and A. Bott (2007): Radiation in the Atmosphere – A Course in Theoretical Meteorology. Cambridge University Press, New York.

Zhang, J., L. Bi, J. Liu, R. L. Panetta, P. Yang, and G. W. Kattawar (2016): Optical scattering simulation of ice particle with surface roughness modeled using the Edwards-Wilkinson equation. Journal of Quantitative Spectroscopy and Radiative Transfer 178, pp. 325-335. doi:10.1016/j.jqsrt.2016.02.013